On the Modelling of the Feeds for Integrated Lens Antennas

By

Cesare Tadolini

in partial fulfilment of the requirements for the degree of

Master of Science
in Electrical Engineering

at the Delft University of Technology,
to be defended publicly on Thursday, February 29, 2024, at 9:00 AM.

Supervisor:	Prof. dr. A. Neto	
Thesis committee:	Prof. dr. A. Neto,	TU Delft
	Dr. D. Cavallo,	TU Delft
	Dr. M. Spirito,	TU Delft

TU Delft

Contents

1 Introduction

The analysis of integrated front ends operated in the high-frequency regimes is addressed in this work. The analysis of these problems has been a critical bottleneck for decades due to the difficulties arising in adopting full-wave techniques. Assuming, as typical at lower frequencies, that the structures are planar leads to the inaccurate representation of some characteristic reactive behaviors. As a case in point, the characteristic impedance of transmission lines, whose thickness is comparable to the width, is not well represented by planar tools. Moreover, existing analytic formulas based on quasi-static approximations for the surrounding fields typically fail when the dynamic components of the fields are also affected by the stratifications.

In this thesis, planar stratified media with transmission lines and radiators are considered to be part of the front end, with this latter being integrated (or in package) thanks to the systematic presence of a dielectric lens antenna. The state of the art of analysing these structures usually resorts to Physical Optics for studying the lenses. Here, state-of-the-art is pushed by introducing the use of the Method of Moments for both the circuitry and the lens, significantly improving the capacity to describe radiation patterns and input impedances well.

While full-wave analysis with commercial tools is already possible, i.e., CST [1], the tool developed here leads to comparable, if not lower, calculation times for realistic antenna configurations. Given the Volumetric Method of Moments (V-MoM) [2] developed in house, this is a significant achievement. To obtain these results, a strategy of “divide et impera” [Filippo II di Macedonia] has been adopted. The analysis of the lens antenna is performed with the V-MoM. It adopts a coarse discretization which is sufficient to describe the low spectral components of the propagating fields within the lens. Next, the antennas feeding the lens are studied separately, assuming the antennas operate in the presence of an infinite dielectric instead of a finite lens. The latter can be evaluated in different ways: with a commercial full-wave solver, with the V-MoM using the appropriate mesh required to represent well the higher spectral components of the near fields, or, in the case of a dipole, with an analytical method also proposed in this work. Finally, the two problems, the feed in the presence of the infinite dielectric and the finite lens, are united to derive the input impedance of the feed of the integrated lens antenna.

This strategy requires the capability to neatly separate the low and high spectral components of the fields of the feed. To this goal, a procedure to evaluate and isolate the mentioned spectral components of the field is proposed. The current on a finite dipole is studied in depth first, and it is shown that it can be separated in the two mentioned spectra for the first time.

The “divide et impera” procedure, is applied not only to a single dipole but to an array of dipoles, with thickness accounted for, operating both in focus or out of the focus of a dielectric lens.

The thesis is structured as follows.

Chapter 2 provides a background on the V-MoM. First, the Volume Equivalence Theorem [3] is used to set an Electric Field Integral Equations (EFIE) and how it can be written in a matrix form with the method of moments [4]. Secondly, it is explained how the 6-D integrals of the EFIE are reduced to 4-D integrals. Next, the Conjugate Gradient method [5] together with the Fast Fourier Transform is used to solve the linear system.

Chapter 3, the main core of this work, explains how to separate the analysis of the feed radiating in the absence of the lens from the interaction between the feed and the lens. This method has been called ‘the auxiliary sources method’ as an auxiliary feed is used to estimate the reflections from the lens surface.

Chapter 4 proposes a novel analytical method to study the input impedance and the current distribution of a dipole exited with a δ-gap generator embedded in a stratified media. This method is based on the Green’s function of an infinite dipole introduced in [6]. The strength of this method is that it allows a deep understanding of the different spectral components of the current: the lower part of the spectrum, which is responsible for radiation, and the higher part, which is associated with capacitive effects.

Chapter 5 concludes the thesis with a summary and proposes some improvements for the V-MoM and for the analytical analysis of the feed.

2 Background on the Volumetric Method of Moments

In this chapter, an overview of the Volumetric Method of Moments (V-MoM), developed for the first time in [2] and [14] and optimized in [7], will be provided. The V-MoM aims to find the equivalent currents of the Volume Equivalence Theorem [3] by solving an electric field integral equation (EFIE). For this purpose, the domain is discretized into a structured grid (i.e., a grid whose points can be ordered in a regular Cartesian structure), and the equivalent currents are represented as constant piece-wise basis functions on the voxels of the grid. The EFIE can then be rewritten in a matrix form, and the unknown equivalent currents can be found by solving a linear system. Due to the many unknowns, the linear system cannot be solved by factorizing the matrix. Thus, the Conjugate Gradient (CG) iterative method [5] is used. Moreover, the matrix product needed in the CG can be calculated for the structured grid using the Fast Fourier Transform (FFT).

The structured grid, together with the piece-wise basis functions, leads to several advantages. First, the reaction integrals of the EFIE can be reused for different problems as they do not depend on the unknowns. Secondly, the number of integrals to be computed and stored is reduced significantly as the linear system matrix has a Toeplitz structure. Finally, the matrix product can be calculated with the help of the FFT, which decreases the computational time.

This Chapter is organized as follows. In Section 2.1, the Volume Equivalence Theorem is applied to derive the EFIE. In Section 2.2, the EFIE is converted into a linear system by expanding the equivalent currents in piece-wise basis functions. In Section 2.3, it is explained how the 6D integral of the EFIE can be reduced to a 4D integral by invoking the equivalence theorem and the appropriate differential relations. In Section 2.4, it is explained how the linear system is solved using the CG method, how the matrix product can be evaluated with the FFT, and how the reaction integrals are computed.

2.1 Derivation of the Volume Integral Equation

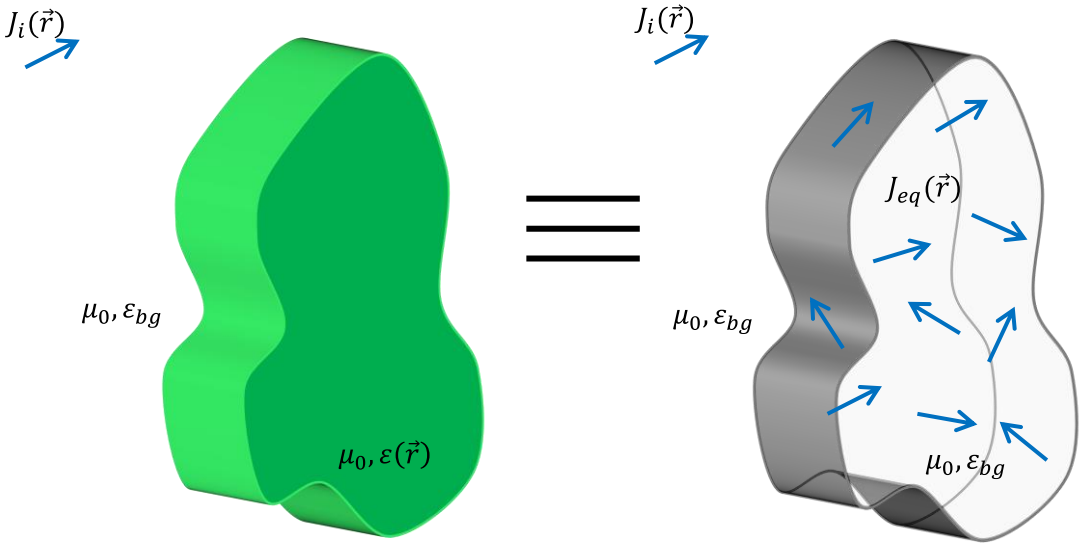

Fig. 2.1. Illustration of the volume equivalence theorem. The obstacle (green body) is replaced by equivalent currents radiating in a homogenous medium

This section explains how to derive the Volume Integral Equation for a scenario when a set of arbitrary sources radiate in the presence of an obstacle. This is achieved by applying the Volume Equivalence Theorem [3], which states that the field disturbances caused by the obstacle can be replaced by equivalent currents radiating in a homogenous space.

Let us introduce a set of arbitrary sources $\vec{J}_i(\vec{r})$ immersed in a homogenous medium of permittivity ε_{bg} and permeability μ_{bg}, which radiate in the presence of an obstacle of volume V and characterized by permittivity $\varepsilon(\vec{r})$ and relative permeability $\mu(\vec{r})$. This scenario is depicted in Fig. 2.1.

By using the superposition principle, the total field can be written as follows:

$$\vec{E}(\vec{r}) = \vec{E}_i(\vec{r}) + \vec{E}_s(\vec{r}) \tag{2.1}$$

$$\vec{H}(\vec{r}) = \vec{H}_i(\vec{r}) + \vec{H}_s(\vec{r}) \tag{2.2}$$

where $\vec{E}_i(\vec{r}), \vec{H}_i(\vec{r})$ are the fields radiated in the absence of the obstacle by the sources $\vec{J}_i(\vec{r})$, and $\vec{E}(\vec{r}), \vec{H}(\vec{r})$ are the total fields, and $\vec{E}_s(\vec{r}), \vec{H}_s(\vec{r})$ are the scattered fields.

As the incident fields are defined in absence of the scatterer, they satisfy the following equations

$$\nabla \times \vec{H}_i(\vec{r}) = \vec{J}_i(\vec{r}) + j\omega\varepsilon_{bg}\vec{E}_i(\vec{r}) \tag{2.3}$$

$$\nabla \times \vec{E}_i(\vec{r}) = -j\omega\mu_{bg}\vec{H}_i(\vec{r}) \tag{2.4}$$

while the total fields satisfy the equations

$$\nabla \times \vec{H}(\vec{r}) = \vec{J}_i(\vec{r}) + j\omega\varepsilon(\vec{r})\vec{E}(\vec{r}) \tag{2.5}$$

$$\nabla \times \vec{E}(\vec{r}) = -j\omega\mu(\vec{r})\vec{H}(\vec{r}) \tag{2.6}$$

By subtracting (2.3) from (2.5) and (2.4) from (2.6) and making use of (2.1)-(2.2) we can write the following identities for the scattered fields

$$\nabla \times \vec{H}_s(\vec{r}) = j\omega\big(\varepsilon(\vec{r}) - \varepsilon_{bg}\big)\vec{E}(\vec{r}) + j\omega\varepsilon_{bg}\vec{E}_s(\vec{r}) \tag{2.7}$$

$$\nabla \times \vec{E}_s(\vec{r}) = -j\omega\big(\mu(\vec{r}) - \mu_{bg}\big)\vec{H}(\vec{r}) - j\omega\mu_{bg}\vec{H}_s(\vec{r}) \tag{2.8}$$

Next, a set of electric and magnetic equivalent currents is introduced

$$\vec{J}_{eq}(\vec{r}) = j\omega\big(\varepsilon(\vec{r}) - \varepsilon_{bg}\big)\vec{E}(\vec{r}) \tag{2.9}$$

$$\vec{M}_{eq}(\vec{r}) = j\omega\big(\mu(\vec{r}) - \mu_{bg}\big)\vec{H}(\vec{r}) \tag{2.10}$$

which are defined only on the volume V enclosing the obstacle. By substituting (2.9) in (2.7) and (2.10) in (2.8), we obtain the Ampere-maxwell Law and Faraday's Law for the scattered fields

$$\nabla \times \vec{H}_s(\vec{r}) = \vec{J}_{eq}(\vec{r}) + j\omega\varepsilon_{bg}\vec{E}_s(\vec{r}) \tag{2.11}$$

$$\nabla \times \vec{E}_s(\vec{r}) = -\vec{M}_{eq}(\vec{r}) - j\omega\mu_{bg}\vec{H}_s(\vec{r}) \tag{2.12}$$

By comparing (2.7)-(2.8) with (2.3)-(2.4), the scattered fields can be seen as the fields radiated by the sources $\vec{J}_{eq}(\vec{r})$, $\vec{M}_{eq}(\vec{r})$ in the homogenous media with permittivity ε_{bg} and permeability μ_{bg}. As in this thesis, only non-magnetic materials (i.e., characterized by permeability $\mu(\vec{r}) = \mu_{bg} = \mu_0$) are considered, (2.10) vanishes, and therefore, only the electric currents $\vec{J}_{eq}(\vec{r})$ are used. Next, by using the dyadic Green's functions of the homogenous media, the electric scattered field can be written as follows

$$\vec{E}_s(\vec{r}) = \frac{1}{j\omega\varepsilon_{bg}}\big(k_{bg}^2 + \nabla\nabla\cdot\big)\iiint_V g(\vec{r} - \vec{r}')\vec{J}_{eq}(\vec{r}')\,d\vec{r}' \tag{2.13}$$

where k_{bg} is the wavenumber in the background medium and the scalar Green's function $g_{bg}(\vec{r})$ is defined as follows

$$g(\vec{r}) = \frac{e^{-jk_{bg}|\vec{r}|}}{4\pi|\vec{r}|}. \tag{2.14}$$

By substituting (2.13) and (2.9) in (2.1) one obtains the following integral equation

$$\vec{E}_i(\vec{r}) = \frac{\vec{J}_{eq}(\vec{r})}{j\omega\big(\varepsilon(\vec{r}) - \varepsilon_{bg}\big)} - \frac{1}{j\omega\varepsilon_{bg}}\big(k_{bg}^2 + \nabla\nabla\cdot\big)\iiint_V g(\vec{r} - \vec{r}')\vec{J}_{eq}(\vec{r}')\,d\vec{r}'. \tag{2.15}$$

With the help of the following identity [8]

$$\big(k_{bg}^2 + \nabla\nabla\cdot\big)\iiint_V g(\vec{r} - \vec{r}')\vec{J}_{eq}(\vec{r}')\,d\vec{r}'$$

$$= \nabla \times \nabla \times \iiint_V g(\vec{r} - \vec{r}')\vec{J}_{eq}(\vec{r}')\,d\vec{r}' - \vec{J}_{eq}(\vec{r}) \tag{2.16}$$

the integral equation in (2.15) becomes

$$\frac{j\omega\varepsilon_{bg}\big(\varepsilon(\vec{r})-\varepsilon_{bg}\big)}{\varepsilon(\vec{r})}\vec{E}_i(\vec{r})=\vec{J}_{eq}(\vec{r})-\frac{\varepsilon(\vec{r})-\varepsilon_{bg}}{\varepsilon(\vec{r})}\nabla\times\nabla\times\iiint_V g(\vec{r}-\vec{r}')\vec{J}_{eq}(\vec{r}')d\vec{r}' \tag{2.17}$$

Where the unknown function is $\vec{J}_{eq}(\vec{r})$.

2.2 Solving the Integral Equation with the MoM

2.2.1 Expansion of the equivalent currents and Galerkin's projection

the integral equation (2.17) can be solved with the method of moments [4], where the unknown is expanded in a set of N_t basis functions $b_1(\vec{r})$, $b_2(\vec{r})$, $b_3(\vec{r})$, ... as follows

$$\vec{J}_{eq}(\vec{r})=\sum_{n=1}^{N_t} i_n\vec{b}_n(\vec{r}). \tag{2.18}$$

Each basis function $\vec{b}_n(\vec{r})$ has a unit of $[1/\mathrm{m}^2]$ and it is weighted by a value i_n [A], so that the equivalent currents $\vec{J}_{eq}(\vec{r})$ have a dimension of $[\mathrm{A}/\mathrm{m}^2]$. For the sake of simplicity, constant piecewise functions are employed. The domain is discretized into $N_s=N_t/3$ cuboids where the current is oriented along $\hat{x},\hat{y},\hat{z}$. $\vec{b}_n(\vec{r})$ is defined as follows

$$\vec{b}_n(\vec{r})=\frac{1}{\Delta^2}\mathrm{rect}\Big(\frac{x-x_m}{\Delta}\Big)\mathrm{rect}\Big(\frac{y-y_m}{\Delta}\Big)\mathrm{rect}\Big(\frac{z-z_m}{\Delta}\Big)\hat{p}_n, \tag{2.19}$$

where $\hat{p}_n\in\{\hat{x},\hat{y},\hat{z}\}$. We define the inner product as follows

$$\langle\vec{f}(\vec{r}),\vec{g}(\vec{r})\rangle_V=\iiint_V\vec{f}(\vec{r})\cdot\vec{g}^*(\vec{r})d\vec{r} \tag{2.20}$$

which yields orthogonality properties between the basis functions.
Then, by substituting (2.18) into (2.17) the integral equation becomes as follows

$$\frac{j\omega\varepsilon_{bg}\big(\varepsilon(\vec{r})-\varepsilon_{bg}\big)}{\varepsilon(\vec{r})}\vec{E}_i(\vec{r})=\sum_{n=1}^{N_t} i_n\left[\vec{b}_n(\vec{r})-\frac{\varepsilon(\vec{r})-\varepsilon_{bg}}{\varepsilon(\vec{r})}\nabla\times\nabla\times\iiint_V g(\vec{r}-\vec{r}')\vec{b}_n(\vec{r}')d\vec{r}'\right] \tag{2.21}$$

where the weights i_n must be determined. By applying Galerkin's method, test functions $\vec{t}_m(\vec{r})=\vec{b}_m(\vec{r})$ are projected into (2.21), which becomes as follows

$$\langle \frac{j\omega\varepsilon_{bg}\left(\varepsilon(\vec{r})-\varepsilon_{bg}\right)}{\varepsilon(\vec{r})}\vec{E}_i(\vec{r}),\vec{b}_m(\vec{r})\rangle_V$$
$$=\langle\sum_{n=1}^{N_t} i_n\left[\vec{b}_n(\vec{r})-\frac{\varepsilon(\vec{r})-\varepsilon_{bg}}{\varepsilon(\vec{r})}\nabla\times\nabla\times\iiint_V g(\vec{r}-\vec{r}')\vec{b}_n(\vec{r}')d\vec{r}'\right],\vec{b}_m(\vec{r})\rangle_V. \tag{2.22}$$

This latter can be written in the following matrix form

$$\mathbf{v}=\left(\frac{\mathbf{I}}{\Delta}-\mathbf{Z^{mat}Z^{rad}}\right)\mathbf{i} \tag{2.23}$$

where $\mathbf{v}$ is the excitation vector whose entries are defined as follows

$$v_m=\langle\frac{j\omega\varepsilon_{bg}\left(\varepsilon(\vec{r})-\varepsilon_{bg}\right)}{\varepsilon(\vec{r})}\vec{E}_i(\vec{r}),\vec{b}_m(\vec{r})\rangle_V=\frac{j\omega\varepsilon_{bg}\left(\varepsilon(\vec{r})-\varepsilon_{bg}\right)}{\varepsilon(\vec{r})}\vec{E}_i(\vec{r})\cdot\hat{p}_m(\vec{r})\Delta$$
$$=\frac{j\omega\varepsilon_{bg}\left(\varepsilon(\vec{r})-\varepsilon_{bg}\right)}{\varepsilon(\vec{r})}e_m\Delta \tag{2.24}$$

where e_m is the average value of $\vec{E}_i$ in the basis function.
Where $\mathbf{Z^{mat}}$ is the following diagonal matrix

$$\mathbf{Z^{mat}}=\mathrm{diag}\left(\frac{\varepsilon_1-\varepsilon_{bg}}{\varepsilon_1},\frac{\varepsilon_2-\varepsilon_{bg}}{\varepsilon_2},\ldots,\frac{\varepsilon_{N_t}-\varepsilon_{bg}}{\varepsilon_{N_t}}\right) \tag{2.25}$$

with ε_1, ε_2, ..., ε_{N_t} being the electric permittivities of the voxels and finally the radiation matrix $\mathbf{Z_{rad}}$ whose entries are given by the following 6D-integral

$$\mathrm{Z}_{mn}^{\mathrm{rad}}=\iiint_{V_m}\vec{b}_m(\vec{r})\cdot\nabla\times\left(\nabla\times\iiint_{V_n} g(\vec{r}-\vec{r}')\vec{b}_n(\vec{r}')d\vec{r}\,d\vec{r}'\right) \tag{2.26}$$

where V_m and V_n are the supports of the test and basis functions, respectively.
As the basis functions are ordered as follows

$$\vec{b}_n(\vec{r})=\vec{b}_m(\vec{r})$$
$$=\underbrace{\vec{b}_1(\vec{r}),\ldots,\vec{b}_{N_t}(\vec{r})}_{\hat{x}-\text{polarized}},\underbrace{\vec{b}_{N_t+1}(\vec{r}),\ldots,\vec{b}_{2N_t}(\vec{r})}_{\hat{y}-\text{polarized}},\underbrace{\vec{b}_{2N_t+1}(\vec{r}),\ldots,\vec{b}_{3N_t=N_s}(\vec{r})}_{\hat{z}-\text{polarized}} \tag{2.27}$$

(2.23) can expanded in the following form

$$\begin{bmatrix}\mathbf{v}_\mathrm{x}\\ \mathbf{v}_\mathrm{y}\\ \mathbf{v}_\mathrm{z}\end{bmatrix}=\left(\frac{\mathbf{I}}{\Delta}-\mathbf{Z^{mat}}\begin{bmatrix}\mathbf{Z}_{\mathbf{rad}}^{xx} & \mathbf{Z}_{\mathbf{rad}}^{xy} & \mathbf{Z}_{\mathbf{rad}}^{xz}\\ \mathbf{Z}_{\mathbf{rad}}^{yx} & \mathbf{Z}_{\mathbf{rad}}^{yy} & \mathbf{Z}_{\mathbf{rad}}^{yz}\\ \mathbf{Z}_{\mathbf{rad}}^{zx} & \mathbf{Z}_{\mathbf{rad}}^{zy} & \mathbf{Z}_{\mathbf{rad}}^{zz}\end{bmatrix}\right)\begin{bmatrix}\mathbf{i}_\mathrm{x}\\ \mathbf{i}_\mathrm{y}\\ \mathbf{i}_\mathrm{z}\end{bmatrix} \tag{2.28}$$

where each $\mathbf{Z}_{\mathbf{rad}}^{kl}$ term is a square matrix, whose entries are projections between the k-polarized test functions and the l-polarized basis functions.

2.3 Reaction Integrals

2.3.1 Reduction from a 6D integral to a 4D integral

The operation "$\nabla \times \nabla \times$ " on the Green's function $g(\vec{r} - \vec{r}')$ in (2.26) leads to a singularity of the order $1/r^3$ which is difficult to treat numerically. In this subsection it is explained how the singularity $1/r^3$ can be reduced to a singularity of the kind $1/r$.
By applying one of the differential relations $\vec{b} \cdot \nabla \times \vec{a} = -\nabla \cdot (\vec{a} \times \vec{b}) - \vec{a} \cdot \nabla \times \vec{b}$, the right hand side of (2.26) becomes as follows

$$
\begin{aligned}
&-\iiint_{V_m} \nabla \cdot \left(\vec{b}_m(\vec{r}) \times \nabla \times \iiint_{V_n} g(\vec{r} - \vec{r}') \vec{b}_n(\vec{r}') d\vec{r}\, d\vec{r}' \right) \\
&-\iiint_{V_m} \nabla \times \vec{b}_m(\vec{r}) \cdot \left(\nabla \times \iiint_{V_n} g(\vec{r} - \vec{r}') \vec{b}_n(\vec{r}') d\vec{r} d\vec{r}' \right)
\end{aligned}
\tag{2.29}
$$

where second term vanishes, being $\vec{b}_m(\vec{r})$ a piecewise constant function. By applying the divergence theorem to the first term of (2.29), the volume integral on V_m can be transformed in the flux through S_m, which is the surface enclosing V_m. Therefore, (2.29) becomes as follows

$$
-\oiint_{S_m} \left[\vec{b}_m(\vec{r}) \times \left(\nabla \times \iiint_{V_n} g(\vec{r} - \vec{r}') \vec{b}_n(\vec{r}') d\vec{r}\,' \right) \right] \cdot \hat{n}_{S_\mathrm{m}}\, dS_\mathrm{m} \tag{2.30}
$$

where $\hat{n}_{S_m}$ is the outwardly oriented normal unit vector of S_m. By permuting the vectors in the triple product, and by taking the operator "$\nabla \times$ " inside the volume integral, (2.30) is rewritten as follows:

$$
-\oiint_{S_m} \left(\hat{n}_{S_m} \times \vec{b}_m(\vec{r}) \right) \cdot \iiint_{V_n} \nabla \times \left(g(\vec{r} - \vec{r}') \vec{b}_n(\vec{r}') \right) d\vec{r}'\, dS_\mathrm{m}. \tag{2.31}
$$

Resorting to the well-known differential relation $\nabla \times (a\, \vec{b}) = a \nabla \times \vec{b} + \nabla a \times \vec{b}$, (2.31) can be written as follows

$$
\begin{aligned}
&-\oiint_{S_m} \left(\hat{n}_{S_m} \times \vec{b}_m(\vec{r}) \right) \\
&\qquad \cdot \iiint_{V_n} \left[g(\vec{r} - \vec{r}') \nabla \times \vec{b}_n(\vec{r}') + \nabla g(\vec{r} - \vec{r}') \times \vec{b}_n(\vec{r}') \right] d\vec{r}'\, dS_m.
\end{aligned}
\tag{2.32}
$$

And, as the differential operator "$\nabla \times$ " is calculated with respect to $\vec{r}$, $\nabla \times \vec{b}_n(\vec{r}')$ vanishes and (2.32) becomes as follows

$$-\oiint_{S_m} \left(\hat{n}_{S_m} \times \vec{b}_m(\vec{r})\right) \cdot \iiint_{V_n} \nabla g(\vec{r} - \vec{r}') \times \vec{b}_n(\vec{r}') d\vec{r}' \, dS_m. \tag{2.33}$$

Since $\vec{b}_m(\vec{r})$ and $\vec{b}_n(\vec{r})$ are piecewise constant functions with polarization $\hat{p}_m$ and $\hat{p}_n$, respectively, (2.33) can be rewritten in the following manner

$$-\frac{1}{\Delta^4} \oiint_{S_m} \left(\hat{n}_{S_m} \times \hat{p}_m\right) \cdot \left(\hat{p}_n \times \iiint_{V_n} -\nabla g(\vec{r} - \vec{r}') d\vec{r}' \right) dS_m. \tag{2.34}$$

By making use of the relation $\nabla g(\vec{r} - \vec{r}') = -\nabla' g(\vec{r} - \vec{r}')$, where ∇' is the differentiation with respect to $\vec{r}'$, (2.34) becomes as follows

$$-\frac{1}{\Delta^4} \oiint_{S_m} \left(\hat{n}_{S_m} \times \hat{p}_m\right) \cdot \left(\hat{p}_n \times \iiint_{V_n} \nabla' g(\vec{r} - \vec{r}') d\vec{r}' \right) dS_m. \tag{2.35}$$

Finally, by applying to (2.35) one of the corollaries[1] of the divergence theorem, the volume Integral in (2.35) can be reduced to a surface integral and each entry of the radiation matrix can be calculated as follows

$$\mathrm{Z}_{mn}^{\mathrm{rad}} = -\frac{1}{\Delta^4} \oiint_{S_m} \left(\hat{n}_{S_m} \times \hat{p}_m\right) \cdot \left(\oiint_{S_n} \hat{p}_n \times \hat{n}_{S_n} g(\vec{r} - \vec{r}') dS_n \right) dS_m. \tag{2.36}$$

Thanks to the divergence theorem and the properties of the differential operators, the volume integrals can be transformed into surface integrals. The singularities $1/r^3$ of (2.26) are converted to $1/r$, which are easier to treat numerically.
The integrals over S_n and S_m in (2.36) can be written as the sum of the integrals between the faces of the cube enclosed by S_m and S_n as follows

$$\mathrm{Z}_{mn}^{\mathrm{rad}} = -\sum_{k=1}^{6} \iint_{S_{m,k}} \left(\hat{n}_{m,k} \times \hat{p}_m\right) \cdot \left(\sum_{l=1}^{6} \iint_{S_{n,l}} \left(\hat{p}_n \times \hat{n}_{n,k}\right) g(\vec{r} - \vec{r}') dS_{n,l} \right) dS_{m,k}, \tag{2.37}$$

[1] By applying the divergence theorem to one of the differential identities one obtains

$$\iiint_V \vec{c} \, \nabla f dV = \oiint_S \vec{c} \, f \cdot \hat{n} dS - \iiint_V f \, \nabla \cdot \vec{c} dV.$$

If $\vec{c}$ is a constant

$$\iiint_V \nabla f dV = \oiint_S f \cdot \hat{n} dS$$

where $S_{m,k}$ is face k of S_m and $S_{n,l}$ is face l of $S_{n,l}$ and $\hat{n}_{m,k}$ and $\hat{n}_{n,k}$ are the normal unit vectors of $S_{m,k}$ and $S_{n,l}$, respectively. As $\hat{p}_n \times \hat{n}_{n,k}$ is a constant, it can be taken out of the integral and (2.37) can be written as follows

$$\mathrm{Z}_{mn}^{\mathrm{rad}} = -\sum_{k=1}^{6}\sum_{l=1}^{6}(\hat{n}_k \times \hat{p}_m)\cdot(\hat{p}_n \times \hat{n}_l)I_{mn}^{kl}, \tag{2.38}$$

where the reaction integral I_{mn}^{kl} is as follows

$$I_{mn}^{kl} = \iint_{S_{m,k}}\iint_{S_{n,l}} g(\vec{r}-\vec{r}')dS_{m,k}dS_{n,l}. \tag{2.39}$$

Fig. 2.2 shows a representation of the integral between face $S_{m,\hat{x}}$ (the face of the m_{th} test function with normal $\hat{x}$) and face $S_{n,\hat{z}}$ (the face of the n_{th} basis function with normal $\hat{z}$). Due to the reciprocity it is sufficient to calculate only the entries of $\mathbf{Z}_{\mathbf{rad}}^{xx}$ and $\mathbf{Z}_{\mathbf{rad}}^{xy}$ of (2.28), while the remaining submatrices can be obtained by a proper permutation of the elements. Moreover, it is clear from (2.39) that the entries of $\mathbf{Z}^{\mathbf{rad}}$ do not depend on the absolute location of the test and basis function but only on their relative position and orientation. Consequently, only few elements of $\mathbf{Z}^{\mathbf{rad}}$ should be calculated. How to exploit the symmetries of the structured grid to reduce the number of the integrals to calculate is explained in Section 2.4.

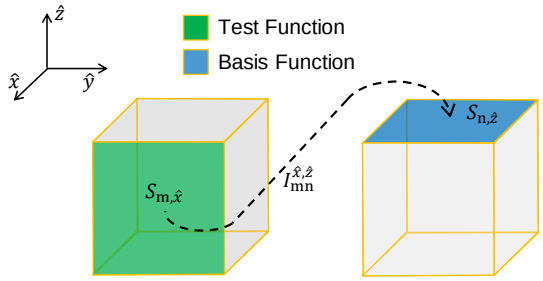

Fig. 2.2. Reaction integral between the face $S_{m,\hat{x}}$ of the test function and face $S_{n,\hat{z}}$ of the basis function.

2.4 Solution

2.4.1 Iterative solver

To calculate the unknowns $\mathbf{i}$ of (2.23), $\left(\mathbf{I}/\Delta - \mathbf{Z}^{\mathbf{mat}}\mathbf{Z}^{\mathbf{rad}}\right)$ must be factorized, but, due its large dimension, this operation is computationally expensive or even prohibitive. Thus, the linear system in (2.23) is solved iteratively by using the CG method[5], one of the most popular method to solve linear system of the form

$$\mathbf{b} = \mathbf{A}\mathbf{x}. \tag{2.40}$$

The fundamental idea behind iterative solvers, such as the Steepest Descent (SD) or CG methods, is that the solution of a system of the kind in (2.40) coincides with the minimum of the quadratic form

$$f(\mathbf{x}) = \frac{1}{2}\left(\mathbf{A^T} + \mathbf{A}\right)\mathbf{x} - \mathbf{b} \tag{2.41}$$

when the matrix $\mathbf{A}$ is positive-definite. The method chosen for the tool is the CG as it needs fewer iterations to converge and it is more accurate than the SD: without considering rounding errors, the CG needs $n = \mathrm{rank}(\mathbf{A})$ steps to find $\min f(\mathbf{x})$, while the rate of convergence of the SD depends on the condition number of $\mathbf{A}$. The CG method starts with an initial guess at the point $\mathbf{x}(0)$ and the next points are iteratively chosen accordingly to

$$\mathbf{x}(i+1) = \mathbf{x}(i) + \alpha(i)\mathbf{d}(i) \tag{2.42}$$

where the scalar $\alpha(i)$ tells how long one should travel along the search direction $\mathbf{d}(i)$ starting from the point $\mathbf{x}(i)$ in order to find the next point $\mathbf{x}(i+1)$. In the SD the search direction $\mathbf{d}(i)$ corresponds to the residual $\mathbf{r}(i) = -\nabla f'\left(\mathbf{x}(i)\right)$ and each search direction is orthogonal to the previous one. The concepts behind the CG are that the search directions are A-orthogonal[1] between each other's and that the search direction $\mathbf{d}(i)$ is A-orthogonal to the error $\mathbf{e}(i+1) = \mathbf{x}(i) - \mathbf{x}$, where $\mathbf{x}$ is the exact solution. The most computationally expensive operation of the algorithm, whose flowchart is illustrated in Fig. 2.3, is the matrix product

$$\mathbf{A}\mathbf{d}_{(i)} = \left(\mathbf{I}/\Delta - \mathbf{Z^{mat}}\mathbf{Z^{rad}}\right)\mathbf{d}_{(i)} = \mathbf{d}_{(i)}/\Delta - \underbrace{\mathbf{Z^{mat}}\underbrace{\left(\mathbf{Z^{rad}}\mathbf{d}_{(i)}\right)}_{\mathbb{1}}}_{\mathbb{2}}. \tag{2.43}$$

Product $\mathbb{1}$ requires the storage of N_t^2 elements and to perform N_t^2 operations as $\mathbf{Z^{rad}}$ is a full matrix. On the other hand, product $\mathbb{2}$ requires to store only N_t elements and to perform only N_t operations as $\mathbf{Z^{mat}}$ is the diagonal matrix defined in (2.25).Fortunately, thanks to the symmetry of the geometry and the translation invariance of the homogeneous space Green's function, $\mathbf{Z^{rad}}$ assumes a Toeplitz (or a block Toeplitz) configuration. This allows us to reduce the number of stored elements and to accelerate product $\mathbb{1}$ with the help of the FFT.

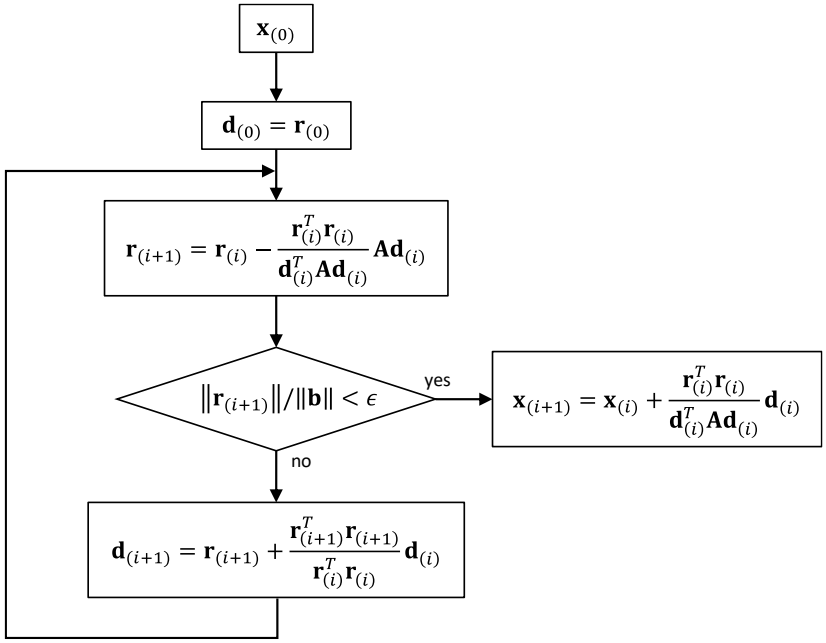

Fig. 2.3. Flowchart of the CG method

2.4.2 Matrix Product with FFT

In this subsection it is explained how to exploit the properties of the Toeplitz or block Toeplitz matrixes to compute a vector product by using the FFT.

List of operations

The followings are three simple operations which are needed to comprehend the content of the subsection

- $\mathbf{B} = [\mathbf{A}]_{a_1:a_2,b_1:b_2,c_1:c_2} \rightarrow$ when $\mathbf{A}$ is a matrix or a tensor, $\mathbf{B}$ is the submatrix (or subtensor) of $\mathbf{A}$, obtained selecting the elements from a_1 to a_2 of the first dimension, from b_1 to b_2 of the second dimension and from c_1 to c_2 of the third dimension
- $\mathbf{B} = \text{reshape}\{\mathbf{A}\}_{N_x,N_y,N_z} \rightarrow$ when $\mathbf{A}$ is a matrix or a tensor composed of $N_x N_y N_z$ element, $\mathbf{B}$ is a $N_x \times N_y \times N_z$ matrix or tensor where the elements of $\mathbf{A}$ are rearranged. The ordering of the elements is carried out along the first dimensions before shifting to the others.
- $\mathbf{B} = \text{flip}(\mathbf{A}) \rightarrow$ when $\mathbf{A}$ is a 2-dimensional matrix, $\mathbf{B}$ is a 2-dimensional matrix obtained by rotating $\mathbf{A}$ clockwise by $180°$.

One Dimensional Geometry

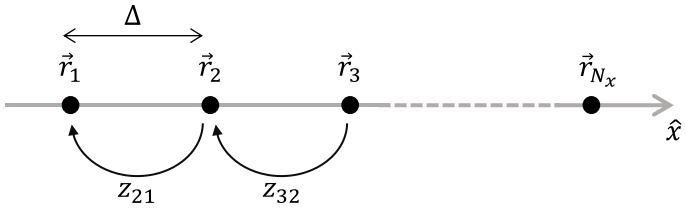

Fig. 2.4. Geometry of N_x equi-spaced basis functions distributed along x-axis.

To make the explanation simpler, one can start by considering a linear problem consisting of N_x equi-spaced elements as shown in Fig. 2.4. For this explanation, the polarization of the basis functions is not relevant and it will be introduced later in this section. The associated radiation matrix can be written as

$$\mathbf{Z}^{\mathbf{rad}} = \begin{bmatrix} z_{11} & z_{12} & z_{13} & \cdots & z_{1N_x} \\ z_{21} & z_{22} & z_{23} & \cdots & z_{2N_x} \\ z_{31} & z_{32} & z_{33} & \cdots & z_{3N_x} \\ \vdots & \vdots & \vdots & \ddots & \vdots \\ z_{N_x1} & z_{N_x2} & z_{N_x3} & \cdots & z_{N_xN_x} \end{bmatrix} \tag{2.44}$$

where z_{11} is the entry representing the field generated by the j_{th} basis function (source) and projected on the i_{th} test function (observation). Because of the space invariance of the homogenous space Green's function, the interaction between basis and test functions depends on their relative position. It follows, for example, that the interaction between the source in r_1 and the observation in r_2 is equal to the interaction between the source in r_2 and the observation in r_3. Each entry can then be written as

$$z_{ij} = z_{j-i} \quad \forall i, j. \tag{2.45}$$

By using the results in (2.45) the radiation matrix becomes as follows

$$\mathbf{Z^{rad}} = \begin{bmatrix} z_0 & z_1 & z_2 & \cdots & z_{N_x-1} \\ z_{-1} & z_0 & z_1 & \cdots & z_{N_x-2} \\ z_{-2} & z_{-1} & z_0 & \cdots & z_{N_x-3} \\ \vdots & \vdots & \vdots & \ddots & \vdots \\ z_{1-N_x} & z_{2-N_x} & z_{3-N_x} & \cdots & z_0 \end{bmatrix} \tag{2.46}$$

which is a Toeplitz matrix, i.e., a matrix where each descending diagonal from left to right is constant. As a Toeplitz matrix is uniquely determined by its first row and first column, it can be characterized by a vector with $2N_x - 1$ entries as follows

$$\dot{\boldsymbol{z}}^{\mathbf{rad}} = [z_{N_x-1} \quad z_{N_x-2} \quad \cdots \quad z_1 \quad z_0 \quad z_{-1} \quad \cdots \quad z_{2-N_x} \quad z_{1-N_x}] \tag{2.47}$$

which reduces the memory requirements from N_x^2 to $2N_x - 1$. To understand how the DFT and the vector $\dot{\boldsymbol{z}}^{\mathbf{rad}}$ can replace the matrix product, it is useful to expressed explicitly the product $\mathbf{Z^{rad}i}$ as follows

$$\mathbf{v} = \mathbf{Z^{rad}i} = \begin{bmatrix} z_0 & z_1 & \cdots & z_{N_x-1} \\ z_{-1} & z_0 & \cdots & z_{N_x-2} \\ \vdots & \vdots & \ddots & \vdots \\ z_{1-N_x} & z_{2-N_x} & \cdots & z_0 \end{bmatrix} \begin{bmatrix} i_1 \\ i_2 \\ \vdots \\ i_{N_x} \end{bmatrix} = \begin{bmatrix} z_0 i_1 + z_1 i_2 + \cdots + z_{N_x-1} i_{N_x} \\ z_{-1} i_1 + z_0 i_2 + \cdots + z_{N_x-2} i_{N_x} \\ \vdots \\ z_{1-N_x} i_1 + z_{2-N_x} i_2 + \cdots + z_0 i_{N_x} \end{bmatrix}. \tag{2.48}$$

One notices that the first element of $\mathbf{v}$ can be obtained by multiplying the first N_x elements of $\dot{\boldsymbol{z}}^{\mathbf{rad}}$ with the elements of $\mathbf{i}$, but with the order reversed:

$$\begin{matrix} z_{N_x-1} & z_{N_x-2} & \cdots & z_1 & z_0 & z_{-1} & \cdots & z_{2-N_x} & z_{1-N_x} \\ i_{N_x} & i_{N_x-1} & \cdots & i_2 & i_1 & & & & \end{matrix}$$

The second element of $\mathbf{v}$ can be obtained by multiplying the elements of $\dot{\boldsymbol{z}}^{\mathbf{rad}}$ from z_{N_x-2} to z_{-1} with the reversed vector $\mathbf{i}$ as shown below

$$\begin{matrix} z_{N_x-1} & z_{N_x-2} & z_{N_x-3} & \cdots & z_0 & z_{-1} & \cdots & z_{2-N_x} & z_{1-N_x} \\ & i_{N_x} & i_{N_x-1} & \cdots & i_2 & i_1 & & & \end{matrix}$$

Similarly, the remaining entries of $\mathbf{v}$ can be obtained by shifting each time the reversed vector $\mathbf{i}$ on the right by one bin. One can recognize this operation as the convolution between $\dot{\boldsymbol{z}}^{\mathbf{rad}}$ and $\mathbf{i}$ and the entries of $\mathbf{v}$ can be obtained by selecting the correct number of elements:

$$\mathbf{v} = \mathbf{Z^{rad}i} = \left[\dot{\boldsymbol{z}}^{\mathbf{rad}} * \mathbf{i}\right]_{N_x:2N_x-1} = \left[\dot{\boldsymbol{z}}^{\mathbf{rad}} \circledast \mathbf{i}^{\mathrm{p}}\right]_{N_x:2N_x-1} \tag{2.49}$$

where $*$ and $\circledast$ denote the convolution and the circular convolutions, respectively, and the vector $\mathbf{i}^{\mathrm{p}}$ is the vector $\mathbf{i}$ padded with $N_x - 1$ at the end

$$\mathbf{i}^{\mathrm{p}} = [\, i_1 \;\; i_2 \;\; i_3 \;\; \ldots \;\; i_{N_x} \; \underbrace{0 \;\; 0 \;\; \ldots \;\; 0}_{N_x-1} \,]^T . \tag{2.50}$$

By recurring to the properties of the circular convolution and the Discrtete Fourier Transform (DFT) the convolution in (2.49) can be calculated as follows

$$\mathbf{v} = \mathbf{Z}^{\mathbf{rad}}\mathbf{i} = \left[\mathrm{IDFT}\left(\mathrm{DFT}\left(\dot{\boldsymbol{z}}^{\mathbf{rad}}\right) \odot \mathrm{DFT}(\mathbf{i}^{\mathrm{p}})\right)\right]_{N_x:2N_x-1} \tag{2.51}$$

where $\odot$ denoted the element-wise multiplication. The DFT can be conveniently calculated with the FFT scaling the computational complexity from $O(N_x^2)$ to $O(N_x \log N_t)$.

Two-Dimensional Geometry

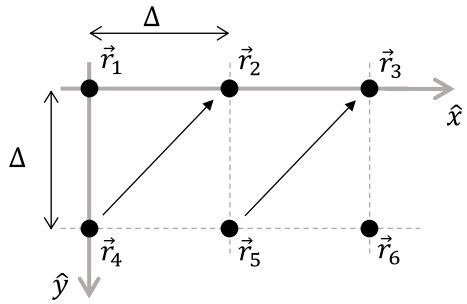

Fig. 2.5. Planar geometry of $N_x = 3$ equi-spaced basis functions along the x-axis and $N_y = 2$ equispaced along the y-axis.

The same approach adopted in the one-dimensional case can be extended to two-dimensions. For the sake of the explanation, let us consider 6 basis functions displaced as shown in Fig. 2.5, with $N_x = 3$ and $N_y = 2$ and with the element numbering carried out along x- before shifting to the next y-coordinate.
As before, the interaction between the test function (observation) and the basis function (source) depends only on their relative position and, for example, z_{35} (field generated by the source located in $\vec{r}_5$ and observed at $\vec{r}_3$) is equal to z_{24} (field generated by the source located in $\vec{r}_4$ and observed at $\vec{r}_2$). Each entry of the radiation matrix can then be rewritten as follows

$$z_{mn} = z_{n_x - m_x, n_y - m_y} \tag{2.52}$$

where (m_x, m_y) and (n_x, n_y) are the coordinates of the observation and the source, respectively, relative to the vector space $\{\Delta\hat{x},\ \Delta\hat{y}\}$. For the simple geometry in Fig. 2.4, the radiation matrix can be written as follows

$$\mathbf{Z}^{\mathbf{rad}} = \left[\begin{array}{ccc|ccc} z_{0,0} & z_{1,0} & z_{2,0} & z_{0,1} & z_{1,1} & z_{2,1} \\ z_{-1,0} & z_{0,0} & z_{1,0} & z_{-1,1} & z_{0,1} & z_{1,1} \\ z_{-2,0} & z_{-1,0} & z_{0,0} & z_{-2,1} & z_{-1,1} & z_{0,1} \\ \hline z_{0,-1} & z_{1,-1} & z_{2,-1} & z_{0,0} & z_{1,0} & z_{2,0} \\ z_{-1,-1} & z_{0,-1} & z_{1,-1} & z_{-1,0} & z_{0,0} & z_{1,0} \\ z_{-2,-1} & z_{-1,-1} & z_{0,-1} & z_{-2,0} & z_{-1,0} & z_{0,0} \end{array}\right] = \begin{bmatrix} \mathbf{Z_0} & \mathbf{Z_1} \\ \mathbf{Z_{-1}} & \mathbf{Z_0} \end{bmatrix} \tag{2.53}$$

$\mathbf{Z}^{\mathbf{rad}}$ is a block-Toeplitz matrix because is composed of 4 Toeplitz submatrices $\mathbf{Z}_{\boldsymbol{k}}$, arranged in a Toeplitz fashion. In each block $\mathbf{Z}_{\boldsymbol{k}}$ the pair (m_y,n_y) is fixed as $\mathbf{Z}_{\boldsymbol{k}}$ represents the interactions within the same y coordinate. Therefore, the subscript k of each block $\mathbf{Z}_{\boldsymbol{k}}$ indicates the difference in y between the source and the observation point (i.e. $\mathbf{Z}_{\boldsymbol{k}} = \mathbf{Z}_{\boldsymbol{n_y - m_y}}$). With an element numbering carried out along the x- coordinate and subsequently along the y-coordinate, the radiation matrix for a planar geometry is composed of $N_y \times N_y$ Toeplitz submatrices with size $N_x \times N_x$. $\mathbf{Z}^{\mathbf{rad}}$ is then fully determined if the first column and its first row of blocks (i.e.,$2N_y - 1$ blocks) are known and each block is fully characterized if its first column and its first row are known (i.e., $2N_x - 1$ elements). It follows that the radiation matrix of a two-dimensional geometry is fully determined by $(2N_x - 1)(2N_y - 1)$ elements and not by $(N_x N_y)^2$. Therefore a $(2N_x - 1)(2N_y - 1)$ matrix containing all the elements sufficient to characterize $\mathbf{Z}^{\mathbf{rad}}$ is introduced and it is given by

$$\ddot{\boldsymbol{z}}^{\mathbf{rad}} = \begin{bmatrix} z_{N_x-1,N_y-1} & \cdots & z_{N_x-1,1} & z_{N_x-1,0} & z_{N_x-1,-1} & \cdots & z_{N_x-1,1-N_y} \\ \vdots & \ddots & \vdots & \vdots & \vdots & \iddots & \vdots \\ z_{1,N_y-1} & \cdots & z_{1,1} & z_{1,0} & z_{1,-1} & \cdots & z_{1,1-N_y} \\ z_{0,N_y-1} & \cdots & z_{0,1} & z_{0,0} & z_{0,-1} & \cdots & z_{0,1-N_y} \\ z_{-1,N_y-1} & \cdots & z_{-1,1} & z_{-1,0} & z_{-1,-1} & \cdots & z_{-1,1-N_y} \\ \vdots & \iddots & \vdots & \vdots & \vdots & \ddots & \vdots \\ z_{1-N_x,N_y-1} & \cdots & z_{1-N_x,1} & z_{1-N_x,0} & z_{1-N_x,-1} & \cdots & z_{1-N_x,1-N_y} \end{bmatrix}. \tag{2.54}$$

For the geometry in Fig. 2.5 the $\ddot{\boldsymbol{z}}^{\mathbf{rad}}$ is as follows

$$\ddot{\boldsymbol{z}}^{\mathbf{rad}} = \begin{bmatrix} z_{2,1} & z_{2,0} & z_{2,-1} \\ z_{1,1} & z_{1,0} & z_{1,-1} \\ z_{0,1} & z_{0,0} & z_{0,-1} \\ z_{-1,1} & z_{-1,0} & z_{-1,-1} \\ z_{-2,1} & z_{-2,0} & z_{-2,-1} \end{bmatrix} \tag{2.55}$$

where each column characterizes a specific submatrix $\mathbf{Z}_{\boldsymbol{k}}$.In particular, the j_{th} column of $\ddot{\boldsymbol{z}}^{\mathbf{rad}}$ represents the submatrix $\mathbf{Z}_{\boldsymbol{N_y - j_{th}}}$.The way each column of $\ddot{\boldsymbol{z}}^{\mathbf{rad}}$ is constructed from its associated submatrix $\mathbf{Z}_{\boldsymbol{k}}$ is the same as $\dot{\boldsymbol{z}}^{\mathbf{rad}}$ is built from $\mathbf{Z}^{\mathbf{rad}}$ in the one-dimensional geometry as explained in (2.46) and (2.47).The product between $\mathbf{Z}^{\mathbf{rad}}$ and $\mathbf{i}$ is as follows

$$\begin{aligned} \mathbf{v} = \mathbf{Z}^{\mathbf{rad}}\mathbf{i} &= \begin{bmatrix} z_{0,0} & z_{1,0} & z_{2,0} & z_{0,1} & z_{1,1} & z_{2,1} \\ z_{-1,0} & z_{0,0} & z_{1,0} & z_{-1,1} & z_{0,1} & z_{1,1} \\ z_{-2,0} & z_{-1,0} & z_{0,0} & z_{-2,1} & z_{-1,1} & z_{0,1} \\ z_{0,-1} & z_{1,-1} & z_{2,-1} & z_{0,0} & z_{1,0} & z_{2,0} \\ z_{-1,-1} & z_{0,-1} & z_{1,-1} & z_{-1,0} & z_{0,0} & z_{1,0} \\ z_{-2,-1} & z_{-1,-1} & z_{0,-1} & z_{-2,0} & z_{-1,0} & z_{0,0} \end{bmatrix} \begin{bmatrix} i_1 \\ i_2 \\ i_3 \\ i_4 \\ i_5 \\ i_6 \end{bmatrix} \\ &= \begin{bmatrix} z_{0,0}i_1 + z_{1,0}i_2 + z_{2,0}i_3 + z_{0,1}i_4 + z_{1,1}i_5 + z_{2,1}i_6 \\ z_{-1,0}i_1 + z_{0,0}i_2 + z_{1,0}i_3 + z_{-1,1}i_4\, z_{0,1}i_5 + z_{1,1}i_6 \\ z_{-2,0}i_1 + z_{-1,0}i_2 + z_{0,0}i_3 + z_{-2,1}i_4 + z_{-1,1}i_5 + z_{0,1}i_6 \\ z_{0,-1}i_1 + z_{1,-1}i_2 + z_{2,-1}i_3 + z_{0,0}i_4 + z_{1,0}i_5 + z_{2,0}i_6 \\ z_{-1,-1}i_1 + z_{0,-1}i_2 + z_{1,-1}i_3 + z_{-1,0}i_4 + z_{0,0}i_5 + z_{1,0}i_6 \\ z_{-2,-1}i_1 + z_{-1,-1}i_2 + z_{0,-1}i_3 + z_{-2,0}i_4 + z_{-1,0}i_5 + z_{0,0}i_6 \end{bmatrix} \end{aligned} \tag{2.56}$$

which can be calculated in a convolutional manner. In the first place, the vector $\mathbf{i}$ must be reshaped into the following $N_x \times N_y$ matrix

$$\ddot{\mathbf{p}} = \text{reshape}\{\mathbf{i}\}_{N_x,N_y} = \begin{bmatrix} p_{1,1} & p_{1,2} \\ p_{2,1} & p_{2,2} \\ p_{3,1} & p_{3,2} \end{bmatrix} = \begin{bmatrix} i_1 & i_4 \\ i_2 & i_5 \\ i_3 & i_6 \end{bmatrix}. \tag{2.57}$$

In general, for arbitrary values of N_x and N_y the entries of $\ddot{\mathbf{p}}$ are defined as

$$p_{i,j} = i_{(j-1)N_x+i}. \tag{2.58}$$

In this example, by applying the flipping operation to (2.57), the flipped vector $\ddot{\mathbf{p}}$ becomes

$$\ddot{\mathbf{p}}^{\text{flip}} = \text{flip}(\ddot{\mathbf{p}}) = \text{flip}\left(\begin{bmatrix} i_1 & i_4 \\ i_2 & i_5 \\ i_3 & i_6 \end{bmatrix}\right) = \begin{bmatrix} i_6 & i_3 \\ i_5 & i_2 \\ i_4 & i_1 \end{bmatrix}. \tag{2.59}$$

The first element of the vector $\mathbf{v}$ defined in (2.56) is calculated as the element-wise product between the elements of $\ddot{\boldsymbol{z}}^{\mathbf{rad}}$ selected by the sliding window indicated in red and the vector $\ddot{\mathbf{p}}^{\text{flip}}$ as illustrated in the scheme below

$$v_1 \rightarrow \begin{bmatrix} z_{2,1} & z_{2,0} & z_{2,-1} \\ z_{1,1} & z_{1,0} & z_{1,-1} \\ z_{0,1} & z_{0,0} & z_{0,-1} \\ z_{-1,1} & z_{-1,0} & z_{-1,-1} \\ z_{-2,1} & z_{-2,0} & z_{-2,-1} \end{bmatrix} \begin{bmatrix} i_6 & i_3 \\ i_5 & i_2 \\ i_4 & i_1 \end{bmatrix}$$

To calculate the second and third elements, the same operation is performed but the sliding window must be shifted one and two positions down, respectively:

$$v_2 \rightarrow \begin{bmatrix} z_{2,1} & z_{2,0} & z_{2,-1} \\ z_{1,1} & z_{1,0} & z_{1,-1} \\ z_{0,1} & z_{0,0} & z_{0,-1} \\ z_{-1,1} & z_{-1,0} & z_{-1,-1} \\ z_{-2,1} & z_{-2,0} & z_{-2,-1} \end{bmatrix} \begin{bmatrix} i_6 & i_3 \\ i_5 & i_2 \\ i_4 & i_1 \end{bmatrix} \qquad v_3 \rightarrow \begin{bmatrix} z_{2,1} & z_{2,0} & z_{2,-1} \\ z_{1,1} & z_{1,0} & z_{1,-1} \\ z_{0,1} & z_{0,0} & z_{0,-1} \\ z_{-1,1} & z_{-1,0} & z_{-1,-1} \\ z_{-2,1} & z_{-2,0} & z_{-2,-1} \end{bmatrix} \begin{bmatrix} i_6 & i_3 \\ i_5 & i_2 \\ i_4 & i_1 \end{bmatrix}$$

For the fourth element of $\mathbf{v}$, the sliding window is moved up to the top-right and finally, for the fifth and sixth entries, the sliding window is moved down by one and two positions

$$v_4 \rightarrow \begin{bmatrix} z_{2,1} & z_{2,0} & z_{2,-1} \\ z_{1,1} & z_{1,0} & z_{1,-1} \\ z_{0,1} & z_{0,0} & z_{0,-1} \\ z_{-1,1} & z_{-1,0} & z_{-1,-1} \\ z_{-2,1} & z_{-2,0} & z_{-2,-1} \end{bmatrix} \begin{bmatrix} i_6 & i_3 \\ i_5 & i_2 \\ i_4 & i_1 \end{bmatrix}$$

$$v_5 \rightarrow \begin{bmatrix} z_{2,1} & z_{2,0} & z_{2,-1} \\ z_{1,1} & z_{1,0} & z_{1,-1} \\ z_{0,1} & z_{0,0} & z_{0,-1} \\ z_{-1,1} & z_{-1,0} & z_{-1,-1} \\ z_{-2,1} & z_{-2,0} & z_{-2,-1} \end{bmatrix} \begin{bmatrix} i_6 & i_3 \\ i_5 & i_2 \\ i_4 & i_1 \end{bmatrix} \qquad v_6 \rightarrow \begin{bmatrix} z_{2,1} & z_{2,0} & z_{2,-1} \\ z_{1,1} & z_{1,0} & z_{1,-1} \\ z_{0,1} & z_{0,0} & z_{0,-1} \\ z_{-1,1} & z_{-1,0} & z_{-1,-1} \\ z_{-2,1} & z_{-2,0} & z_{-2,-1} \end{bmatrix} \begin{bmatrix} i_6 & i_3 \\ i_5 & i_2 \\ i_4 & i_1 \end{bmatrix}$$

As this operation is the convolution between matrix $\ddot{\mathbf{p}}$ and the matrix $\ddot{\boldsymbol{z}}^{\mathbf{rad}}$,the product in (2.56) can be written as follows

$$\mathbf{v} = \mathrm{reshape}\left\{\left[\ddot{\boldsymbol{z}}^{\mathbf{rad}} * \ddot{\mathbf{p}}\right]_{N_x:2N_x-1,N_y:2N_y-1}\right\}_{1,N_xN_y}. \tag{2.60}$$

Next, a new $(2N_x - 1) \times (2N_y - 1)$ matrix $\ddot{\mathbf{p}}^{\mathrm{p}}$ is built from the matrix $\ddot{\mathbf{p}}$ by adding $N_x - 1$ zeros in the first dimension and $N_y - 1$ zeros in the second dimension as follows

$$\ddot{\mathbf{p}}^{\mathrm{p}} = \begin{bmatrix} p_{1,1} & p_{1,2} & \dots & p_{1,N_y} & 0 & \dots & 0 \\ p_{2,1} & p_{2,2} & \dots & p_{2,N_y} & 0 & \dots & 0 \\ \vdots & \vdots & \ddots & \vdots & 0 & \dots & 0 \\ p_{N_x,1} & p_{N_x,2} & \dots & p_{N_x,N_y} & \vdots & \dots & 0 \\ 0 & 0 & 0 & \dots & 0 & \dots & 0 \\ \vdots & \vdots & \vdots & \vdots & \vdots & \ddots & \vdots \\ 0 & 0 & 0 & 0 & 0 & \dots & 0 \end{bmatrix} \tag{2.61}$$

Finally, by exploiting the DFT properties, the convolution in (2.60) can be written as a product in the frequency domain

$$\mathbf{v} = \mathrm{reshape}\left\{\mathrm{IFFT}\left[\mathrm{FFT}\left(\ddot{\boldsymbol{z}}^{\mathbf{rad}}\right) \odot \mathrm{FFT}(\ddot{\mathbf{p}}^{\mathrm{p}})\right]_{N_x:2N_x-1,N_y:2N_y-1}\right\}_{1,N_xN_y}. \tag{2.62}$$

Three-Dimensional Geometry

The two-dimensional case can be extended to a three-dimensional one without any major effort. The numbering of the basis function is carried out in the xy-plane as in the two-dimensional geometry before shifting to the next z-coordinate.
In this case, the radiation matrix can be written as follows

$$\mathbf{Z}^{\mathbf{rad}} = \begin{bmatrix} \mathbf{Z_0} & \mathbf{Z_1} & \dots & \mathbf{Z}_{N_z-1} \\ \mathbf{Z}_{-1} & \mathbf{Z_0} & \dots & \mathbf{Z}_{N_z-2} \\ \vdots & \vdots & \ddots & \vdots \\ \mathbf{Z}_{1-N_z} & \mathbf{Z}_{2-N_z} & \dots & \mathbf{Z_0} \end{bmatrix}. \tag{2.63}$$

It consists of $(2N_z - 1)$ submatrices $\mathbf{Z_k}$ arranged in a Toeplitz fashion. Each block $\mathbf{Z_k}$ contains the interaction between sources and observations with a fixed distance along the z-axis and it is constructed in the same way $\mathbf{Z}^{\mathbf{rad}}$ is constructed in the two-dimensional case. In this case, a two-dimensional matrix is not sufficient to fully determine the radiation matrix but a $(2N_x - 1) \times (2N_y - 1) \times (2N_z - 1)$ tensor $\ddot{\boldsymbol{z}}^{\mathbf{rad}}$ is needed. To have an expression for the tensor, each element of the radiation matrix must be rewritten as follows

$$z_{mn} = z_{n_x-m_x,n_y-m_y,n_z-m_z}, \tag{2.64}$$

where (m_x, m_y, m_z) and (n_x, n_y, n_z) are the coordinates of the observation and the source, respectively, relative to the vector space $\{\Delta\hat{x},\ \Delta\hat{y},\ \Delta\hat{z}\}$.

The tensor $\ddot{\mathbf{z}}^{\mathbf{rad}}$ consists of $(2N_z - 1)$ 'pages', where, due to the ordering of the elements, each 'page' is filled with the interactions between the source and the observations with the same distance along the z-direction. Each $\ddot{\mathbf{z}}^{\mathbf{rad}}_{\mathrm{page},k}$ is defined as follows

$$\ddot{\mathbf{z}}^{\mathbf{rad}}_{\mathrm{page},k} = \begin{bmatrix} z_{N_x-1,N_y-1,} & \cdots & z_{N_x-1,1} & z_{N_x-1,0} & z_{N_x-1,-1} & \cdots & z_{N_x-1,1-N_y} \\ \vdots & \ddots & \vdots & \vdots & \vdots & \iddots & \vdots \\ z_{1,N_y-1} & \cdots & z_{1,1} & z_{1,0} & z_{1,-1} & \cdots & z_{1,1-N_y} \\ z_{0,N_y-1} & \cdots & z_{0,1} & z_{0,0} & z_{0,-1} & \cdots & z_{0,1-N_y} \\ z_{-1,N_y-1} & \cdots & z_{-1,1} & z_{-1,0} & z_{-1,-1} & \cdots & z_{-1,1-N_y} \\ \vdots & \iddots & \vdots & \vdots & \vdots & \ddots & \vdots \\ z_{1-N_x,N_y-1} & \cdots & z_{1-N_x,1} & z_{1-N_x,0} & z_{1-N_x,-1} & \cdots & z_{1-N_x,1-N_y} \end{bmatrix}. \tag{2.65}$$

As each page is characterized by a fixed distance between source and observations along the z-direction, the third index in the matrix in (2.65) has been omitted. In particular, for the k_{th} page, this distance is $k - N_z$. Next, the vector $\mathbf{i}$ is reshaped to build the $N_x \times N_y \times N_z$ tensor $\ddot{\mathbf{p}}$

$$\ddot{\mathbf{p}} = \mathrm{reshape}\{\mathbf{i}\}_{N_x,N_y,N_z}, \tag{2.66}$$

and each entry of $\ddot{\mathbf{p}}$ are defined as:

$$p_{i,j,k} = i_{(k-1)N_xN_y+(j-1)N_x+i}. \tag{2.67}$$

As for the one- and two- dimensional cases, a new tensor $\ddot{\mathbf{p}}^{\mathrm{p}}$ is built by padding with zeros the tensor $\ddot{\mathbf{p}}$ in order to have the same dimension of the tensor $\ddot{\mathbf{z}}^{\mathbf{rad}}$. The zeros are added at the end of the each dimension so that

$$[\ddot{\mathbf{p}}^{\mathrm{p}}]_{1:N_x,1:N_y,1:N_y} = \ddot{\mathbf{p}}. \tag{2.68}$$

Finally, once that all the necessary components have been defined, the product $\mathbf{Z}^{\mathbf{rad}}\mathbf{i}$ can be calculated with the FFT as follows

$$\mathbf{v} = \mathrm{reshape}\left\{\left[\mathrm{IFFT}\left(\mathrm{FFT}\left(\ddot{\mathbf{z}}^{\mathbf{rad}}\right) \odot \mathrm{FFT}(\mathbf{P}^{\mathrm{p}})\right)\right]_{N_x:2N_x-1,N_y:2N_y-1,N_z:2N_z-1}\right\}_{1,N_xN_yN_z}. \tag{2.69}$$

2.4.3 Polarization of the test and basis functions

Once that the procedure on how the treat Toeplitz or block-Toeplitz matrixes with the DFT has been explained, the polarization of the basis and test functions has to be considered. The product $\mathbb{1}$ in (2.43) can be expanded as follows

$$\mathbf{Z}_{\mathbf{rad}}\mathbf{d}_{(i)} = \begin{bmatrix} \mathbf{Z}^{xx}_{\mathbf{rad}} & \mathbf{Z}^{xy}_{\mathbf{rad}} & \mathbf{Z}^{xz}_{\mathbf{rad}} \\ \mathbf{Z}^{yx}_{\mathbf{rad}} & \mathbf{Z}^{yy}_{\mathbf{rad}} & \mathbf{Z}^{yz}_{\mathbf{rad}} \\ \mathbf{Z}^{zx}_{\mathbf{rad}} & \mathbf{Z}^{zy}_{\mathbf{rad}} & \mathbf{Z}^{zz}_{\mathbf{rad}} \end{bmatrix} \begin{bmatrix} \mathbf{d}^{x}_{(i)} \\ \mathbf{d}^{y}_{(i)} \\ \mathbf{d}^{z}_{(i)} \end{bmatrix} = \begin{bmatrix} \mathbf{Z}^{xx}_{\mathbf{rad}} \\ \mathbf{Z}^{yx}_{\mathbf{rad}} \\ \mathbf{Z}^{zx}_{\mathbf{rad}} \end{bmatrix} \mathbf{d}^{x}_{(i)} + \begin{bmatrix} \mathbf{Z}^{xy}_{\mathbf{rad}} \\ \mathbf{Z}^{yy}_{\mathbf{rad}} \\ \mathbf{Z}^{zy}_{\mathbf{rad}} \end{bmatrix} \mathbf{d}^{y}_{(i)} + \begin{bmatrix} \mathbf{Z}^{xz}_{\mathbf{rad}} \\ \mathbf{Z}^{yz}_{\mathbf{rad}} \\ \mathbf{Z}^{zz}_{\mathbf{rad}} \end{bmatrix} \mathbf{d}^{z}_{(i)} \tag{2.70}$$

Where $\mathbf{Z}_{\mathbf{rad}}^{lk}$ is the radiation matrix of the interaction between k-polarized basis functions and l-polarized test functions and the entries of $\mathbf{Z}_{\mathbf{rad}}^{lk}$ are calculated as in (2.38). Each matrix product $\mathbf{Z}_{\mathbf{rad}}^{lk} \cdot \mathbf{d}_{(i)}^{k}$ is calculated with the FFT as explained earlier. Moreover, if a rectangular grid is considered, due to the symmetry and reciprocity, not all the matrixes $\mathbf{Z}_{\mathbf{rad}}^{lk}$ have to be computed: by knowing the entries of $\mathbf{Z}_{\mathbf{rad}}^{xx}$, $\mathbf{Z}_{\mathbf{rad}}^{yy}$ and $\mathbf{Z}_{\mathbf{rad}}^{zz}$ con be calculated as follows

$$\begin{aligned} \mathrm{Z}_{\mathrm{rad},i,j,k}^{yy} &= \mathrm{Z}_{\mathrm{rad},j,i,k}^{xx} \\ \mathrm{Z}_{\mathrm{rad},i,j,k}^{zz} &= \mathrm{Z}_{\mathrm{rad},k,i,j}^{xx} \end{aligned} \tag{2.71}$$

where the inversion of the subscripts on the right hand side indicates a permutation of the elements. The remaining submatrices can be obtained from $\mathbf{Z}_{\mathbf{rad}}^{xy}$ as follows

$$\begin{aligned} \mathrm{Z}_{\mathrm{rad},i,j,k}^{yx} &= \mathrm{Z}_{\mathrm{rad},i,j,k}^{xy} \\ \mathrm{Z}_{\mathrm{rad},i,j,k}^{zx} = \mathrm{Z}_{\mathrm{rad},i,j,k}^{xz} &= \mathrm{Z}_{\mathrm{rad},i,k,j}^{xy}, \\ \mathrm{Z}_{\mathrm{rad},i,j,k}^{zy} = \mathrm{Z}_{\mathrm{rad},i,j,k}^{yz} &= \mathrm{Z}_{\mathrm{rad},k,i,j}^{xy}. \end{aligned} \tag{2.72}$$

2.4.4 Construction of the coupling tensors

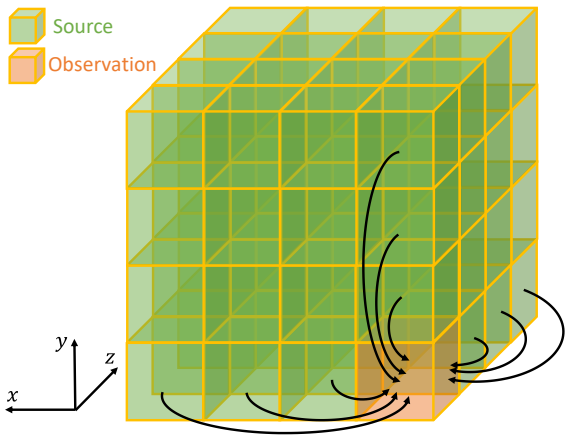

Fig. 2.6. Construction of the tensor by fixing the test function on the first voxel in the grid and sweeping the basis function over all of the voxels within the grid.

The number of entries each tensor is composed of is $(2N_x - 1)(2N_y - 1)(2N_z - 1)$,·but the number of integrals can be reduced to $N_x N_y N_z$. As the magnitude of the reaction integrals depends only on the absolute distance between the test and basis function, the tensor entries in (2.65) follow this relation

$$\left|\ddot{\mathbf{z}}_{\pm i,\pm j,\pm k}^{\mathbf{rad}}\right| = \left|\ddot{\mathbf{z}}_{i,j,k}^{\mathbf{rad}}\right|. \tag{2.73}$$

One can then fix the source (basis function) on the first voxel and sweep the observation (test function) to all the cuboids within the grid a shown in Fig. 2.6. It means that only the entries with $1 \leq i \leq N_x$, $1 \leq j \leq N_y$, $1 \leq k \leq N_z$ in (2.73) should be computed and the remaining entries can be obtained from the calculated ones by correcting the sign.

For the sake of the explanation, one can consider the simple two-dimensional geometry in Fig. 2.5. The associated tensor $\ddot{\boldsymbol{z}}^{\mathbf{rad}}$ is

$$\ddot{\boldsymbol{z}}^{\mathbf{rad}} = \begin{bmatrix} z_{2,1} & z_{2,0} & z_{2,-1} \\ z_{1,1} & z_{1,0} & z_{1,-1} \\ z_{0,1} & z_{0,0} & z_{0,-1} \\ z_{-1,1} & z_{-1,0} & z_{-1,-1} \\ z_{-2,1} & z_{-2,0} & z_{-2,-1} \end{bmatrix}$$

and only the entries encircled in red should be calculated as:

$$\begin{bmatrix} z_{2,-1} \\ z_{1,-1} \\ z_{0,-1} \end{bmatrix} = \begin{bmatrix} z_{2,1} \\ z_{1,1} \\ z_{0,1} \end{bmatrix}, \begin{bmatrix} z_{-1,1} \\ z_{-1,0} \\ z_{-1,-1} \end{bmatrix} = \begin{bmatrix} z_{1,1} \\ z_{1,0} \\ z_{1,-1} \end{bmatrix}, \begin{bmatrix} z_{-2,1} \\ z_{-2,0} \\ z_{-2,-1} \end{bmatrix} = \begin{bmatrix} z_{2,1} \\ z_{2,0} \\ z_{2,-1} \end{bmatrix}$$

for $\ddot{\boldsymbol{z}}^{\mathbf{rad},\hat{x}\hat{x}}$ and

$$\begin{bmatrix} z_{2,-1} \\ z_{1,-1} \\ z_{0,-1} \end{bmatrix} = -\begin{bmatrix} z_{2,1} \\ z_{1,1} \\ z_{0,1} \end{bmatrix}, \begin{bmatrix} z_{-1,1} \\ z_{-1,0} \\ z_{-1,-1} \end{bmatrix} = -\begin{bmatrix} z_{1,1} \\ z_{1,0} \\ z_{1,-1} \end{bmatrix}, \begin{bmatrix} z_{-2,1} \\ z_{-2,0} \\ z_{-2,-1} \end{bmatrix} = -\begin{bmatrix} z_{2,1} \\ z_{2,0} \\ z_{2,-1} \end{bmatrix}$$

for $\ddot{\boldsymbol{z}}^{\mathbf{rad},\hat{x}\hat{y}}$.

Let us focus on the construction on the tensor $\dddot{\boldsymbol{z}}^{\mathbf{rad},\hat{x}\hat{x}}$. By substituting $\hat{p}_m = \hat{p}_n = \hat{x}$ in (2.38) we obtain the following expression

$$\mathrm{Z}_{mn}^{\mathrm{rad}} = -\sum_{k=1}^{6}\sum_{l=1}^{6}(\hat{n}_k \times \hat{x}) \cdot (\hat{x} \times \hat{n}_l) I_{mn}^{kl} \tag{2.74}$$

where only the 8 terms associated with $\hat{n}_k$ and $\hat{n}_l$ are either $\pm\hat{y}$ or $\pm\hat{z}$ are non-zero. To avoid performing the same integral I_{mn}^{kl} multiple times, a tensor $\boldsymbol{z}^{\mathrm{surf},zz}$ is defined, and it is obtained by fixing the observation on the face with $\hat{n}_k = \hat{z}$ of the first voxel and sweeping the source over all the faces with $\hat{n}_l = \hat{z}$ of the other voxels within the domain as shown in Fig. 2.7. Then, the tensor $\dddot{\boldsymbol{z}}^{\mathbf{rad},xx}$ can be calculated as follows

$$\dddot{\boldsymbol{z}}_{i,j,k}^{\mathbf{rad},xx} = 2\boldsymbol{z}_{i,j,k}^{\mathrm{surf},zz} - \boldsymbol{z}_{i,j,k+1}^{\mathrm{surf},zz} - \boldsymbol{z}_{i,j,k-1}^{\mathrm{surf},zz} + 2\boldsymbol{z}_{i,k,j}^{\mathrm{surf},zz} - \boldsymbol{z}_{i,k+1,j}^{\mathrm{surf},zz} - \boldsymbol{z}_{i,k-1,j}^{\mathrm{surf},zz} \tag{2.75}$$

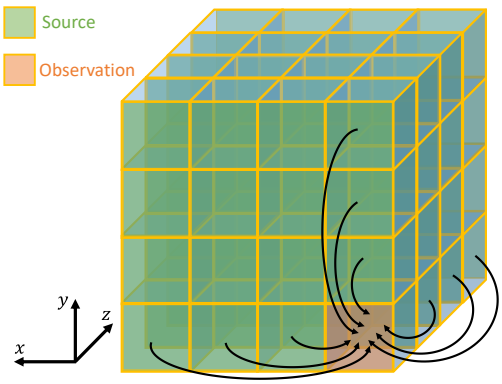

Fig. 2.7. Fixing the observation on the face with $\hat{n}_k = \hat{z}$ of the first voxel and sweeping the source over all the faces with $\hat{n}_l = \hat{z}$ of the other voxels within the domain.

Let us now consider the tensor $\ddot{\boldsymbol{z}}^{\mathbf{rad},\hat{x}\hat{y}}$. By substituting $\hat{p}_m = \hat{x}$ and $\hat{p}_n = \hat{y}$ in (2.38) we obtain the following expression

$$\mathrm{Z}_{mn}^{\mathrm{rad}} = -\sum_{k=1}^{6}\sum_{l=1}^{6}(\hat{n}_k \times \hat{x}) \cdot (\hat{y} \times \hat{n}_l) I_{mn}^{kl}. \tag{2.76}$$

Only 4 terms in the summation do not vanishes as they are nonzero whenever $\hat{n}_k$ and $\hat{n}_l$ are oriented along $\pm\hat{x}$ and $\pm\hat{y}$, respectively. Similar to before, a tensor $\boldsymbol{z}^{\mathrm{surf},yx}$ is calculated by fixing the observation on the face with $\hat{n}_k = \hat{y}$ of the first voxel and sweeping the source over all the faces with $\hat{n}_l = \hat{x}$ of the other voxels. Then, the tensor $\ddot{\boldsymbol{z}}^{\mathbf{rad},xy}$ can be calculated as follows

$$\ddot{\boldsymbol{z}}_{i,j,k}^{\mathbf{rad},xy} = -\boldsymbol{z}_{i,j,k}^{\mathrm{surf},yx} + \boldsymbol{z}_{i,j+1,k}^{\mathrm{surf},yx} + \boldsymbol{z}_{i-1,j,k}^{\mathrm{surf},yx} - \boldsymbol{z}_{i-1,j+1,k}^{\mathrm{surf},yx} \tag{2.77}$$

To calculate the tensors $\boldsymbol{z}^{\mathrm{surf},zz}$ and $\boldsymbol{z}^{\mathrm{surf},yx}$ we need to evaluate the corresponding reaction integrals $I_{i,j,k}^{zz}$ and $I_{i,j,k}^{yx}$. The integrals can be divided into 4 groups:

1. *Non adjacent faces* [Fig. 2.8(a)]: the faces are separated and the double integral can be calculated with the desired quadrature. In this case the singularity of the of $g(\vec{r} - \vec{r}')$ is not in the domain of integration.
2. *Coinciding faces* [Fig. 2.8(b)]: in this case the singularity of $g(\vec{r} - \vec{r}')$ is encountered whenever $\vec{r} - \vec{r}'$.
3. *Vertex-adjacent faces* [Fig. 2.8(c)]: in this case the singularity of $g(\vec{r} - \vec{r}')$ is encountered at the vertex the faces have in common.
4. *Edge-adjacent faces* [Fig. 2.8(d)]: in this case the singularity of $g(\vec{r} - \vec{r}')$ is encountered at the coinciding edge.

The integrals of group 2,3,4 is calculated with DIRECTFN, introduced in [9], [10], where the integral is calculated in polar coordinates so that singularity $1/r$ is cancelled by the Jacobian.

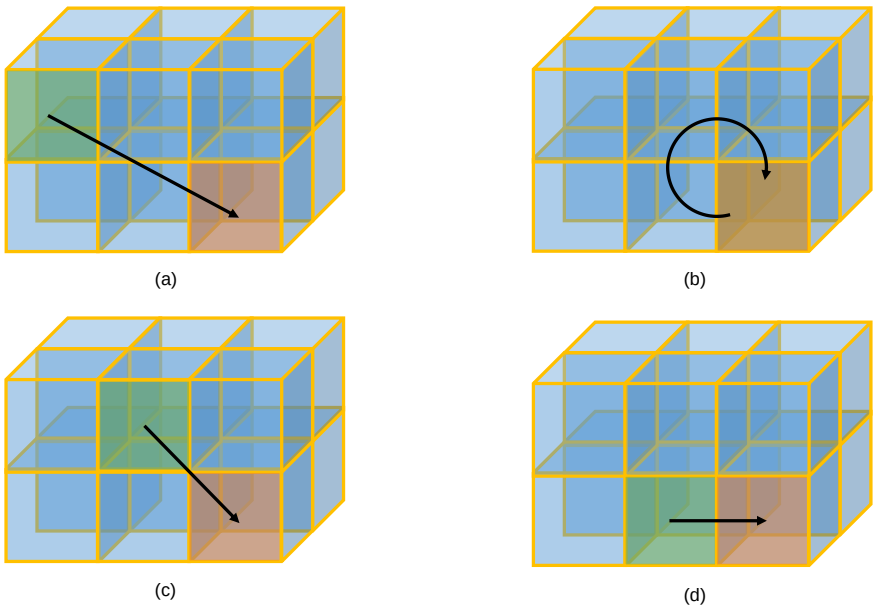

Fig. 2.8. Reaction integral between (a) non-adjacent faces, (b) coinciding faces, (c) vertex-adjacent faces and (d) edge-adjacent faces.

2.5 Validation

2.5.1 Mie Series

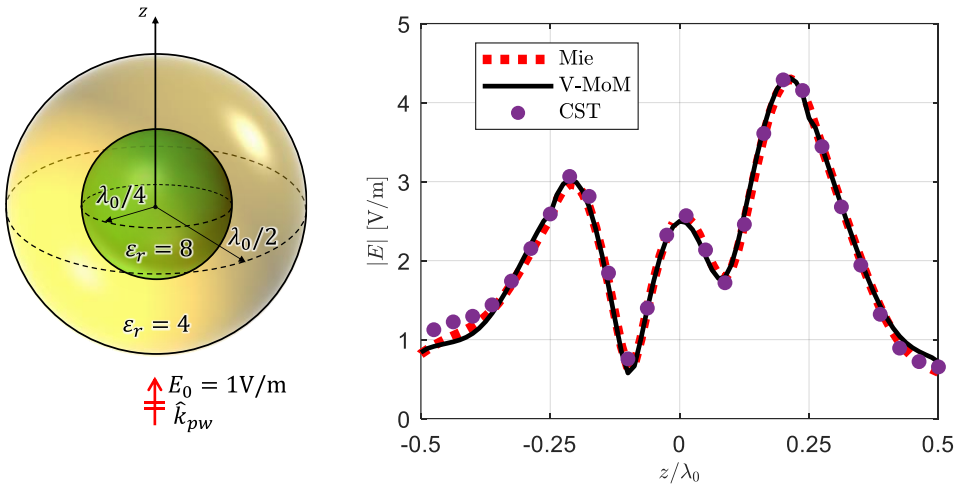

Fig. 2.9. (a) Illustration of a multi-layer sphere consisting of an inner sphere with $R_1 = \lambda_0/4$ and $\varepsilon_r = 8$ and of an external sphere with $R_1 = \lambda_0/4$ and $\varepsilon_r = 4$. (b) Total field along $\hat{z}$ inside the multi-layer sphere obtained with the Mie series, V-MoM and CST.

The V-MoM has been validated against the Mie Series [11], by simulating a multi-layer sphere consisting of an inner sphere with $R_1 = \lambda_0/4$ and $\varepsilon_r = 8$ surrounded by an external sphere with $R_1 = \lambda_0/4$ and $\varepsilon_r = 4$ as shown in Fig. 2.9(a). The body is illuminated by a plane wave with amplitude $\vec{E}_0 = 1\mathrm{V/m}$ coming from the negative z-direction and with the field oriented along $\hat{x}$.The body is discretized into basis function with $\Delta = \lambda_0/80$. Moreover, the V-MoM has been compared with CST in terms of accuracy and computational time. The accuracy of the two numerical solvers is given by the relative error, which is defined as follows

$$\epsilon_{\mathrm{solver}} = \left\| \frac{|\vec{E}_{\mathrm{solver}}| - |\vec{E}_{\mathrm{Mie}}|}{|\vec{E}_{\mathrm{Mie}}|} \right\| \tag{2.78}$$

where $\|\cdot\|$ is the Euclidean Norm. The performance of the two numerical solvers are reported in Table 1. The time to calculate the integrals (34 sec) has not been included In the computational time of the V-MoM, as they can be reused. The V-MoM slightly outperform CST in terms of accuracy and it is also faster as it takes 35 sec to solve the linear system while CST takes almost one minute.

	$\epsilon_{\mathrm{solver}}$	Computation Time
V-MoM	2.87 %	35 sec
CST	3.73 %	53 sec

Table 1: Performance comparison between CST and the V-MoM, CPU: Intel® Core™ i5-12500 3.00GHz, RAM: 16GB.

2.5.2 Input Impedance Dipole

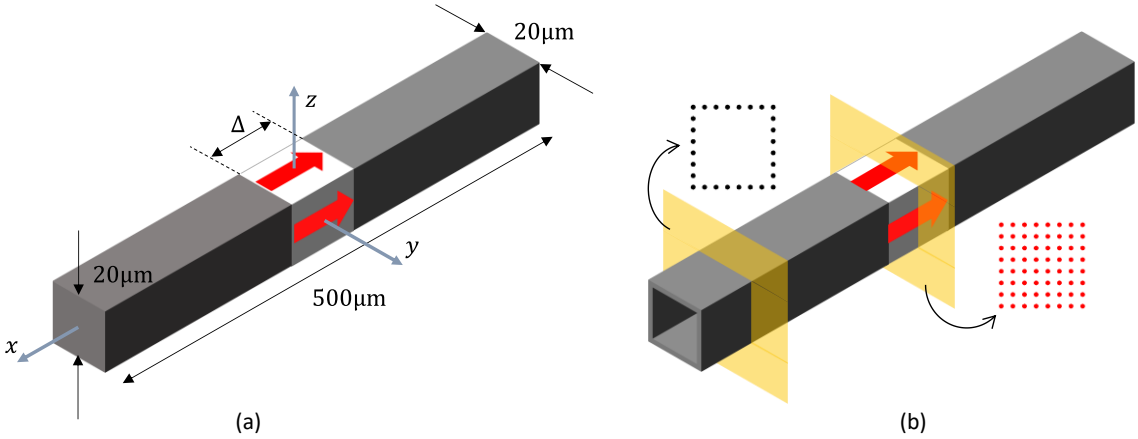

Fig. 2.10. (a) Illustration of the dipole which has been simulated. (b) How the dipole has been modelled with the MoM: the cross section on the arms are empty on the middle while the ones on the gap are completely filled.

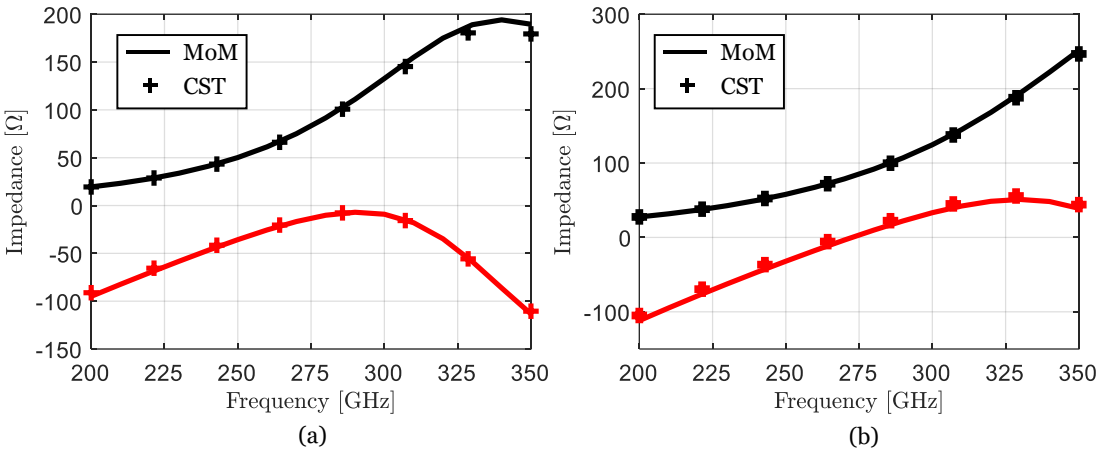

Fig. 2.11. Input impedance of the dipole when exited by a δ-gap generator (a) 2.5μm and (a) 10μm long calculated with V-MoM and CST.

The input impedance of a dipole made of a homogenous media of resistivity $\rho = 10^{-6}\Omega\text{m}$ radiating in free space is simulated with the V-MoM and with CST. The dipole is $500\mu\text{m}$ long, with a square cross-section $20\mu\text{m} \times 20\mu\text{m}$ and with a δ-gap generator Δ long as shown in Fig. 2.10(a). The length of the basis functions is $2.5\mu\text{m}$ so a $200 \times 8 \times 8$ grid is needed to model the dipole with the V-MoM. As, due to the skin effect, the currents are concentrated near the surface, the dipole in the V-MoM has been modelled as in Fig. 2.10(b): while the gap is completely filled with basis functions (i.e., 64 basis functions per cross-section), in the arms of the dipole only the external basis functions are considered (i.e., 28 basis functions per cross section). Thanks to this choice, the stability and the number of iterations is reduced significantly. The volumetric excitation has been modelled in CST with 4 discrete ports between the vertexes of the feeding gap. The Input impedances calculated with CST and with the V-MoM for $\Delta = 2.5\mu\text{m}$ and $10\mu\text{m}$ are illustrated in Fig. 2.11 showing a good agreement.

This example well highlights the flexibility of the V-MoM: once the calculation of the integrals is completed, the V-MoM is very fast to converge. This allows us to quickly study, for example, different gap lengths or dipoles with smaller dimensions by using the

same integrals. The performance of CST and the V-MoM in terms of time are compared in Table 2 for the calculation of the impedance at 300GHz.

	$\Delta = 2.5\mu m$	$\Delta = 10\mu m$
V-MoM +254s for the integrals	7 s	7 s
CST	229 s	224 s

Table 2. Comparison between CST and the V-MoM in terms of computational time for calculating the input impedance at 300GHz. CPU: Intel® Core™ i5-12500 3.00GHz, RAM: 16GB.

3 Reflection Extraction with the Auxiliary Sources Method

3.1 Introduction

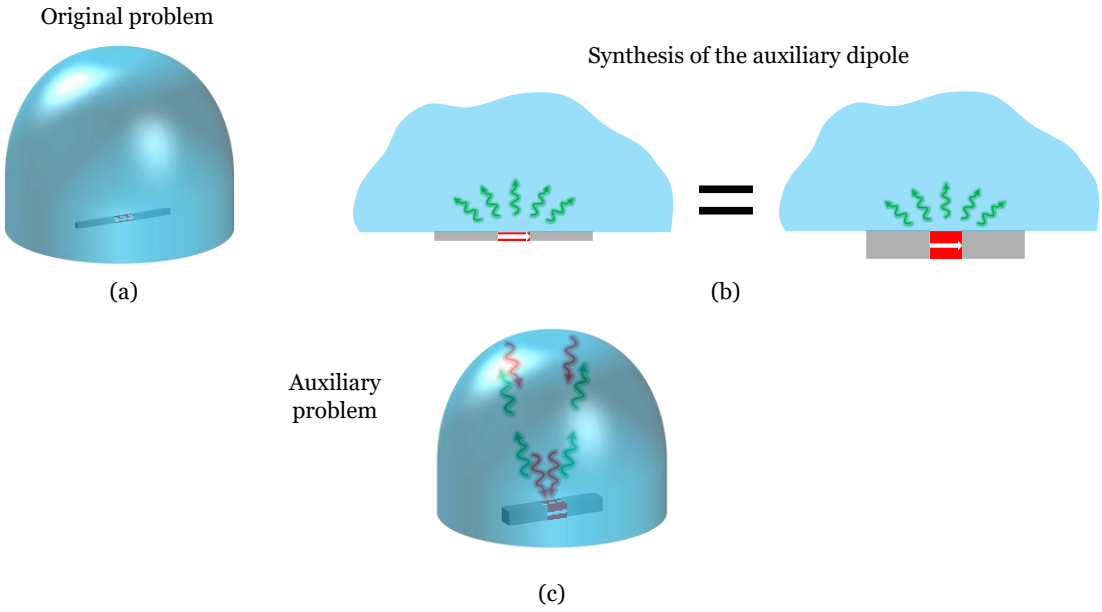

Fig. 3.1: (a) the original problem consists in a lens illuminated by a thin dipole (i.e. the original dipole), characterized by fine details. (b) An auxiliary thicker dipole is synthetized in order to have the same dynamic currents of the original one. (c) The interaction between the lens and the feed can be studied by means of the auxiliary dipole.

In the sub-mm wave domain, some of the most successful examples of front-end integration resort to antennas distributed on the focal planes of dielectric lenses. The analysis and design of such antennas typically require the accurate modeling of the input impedance, mutual coupling, and radiation patterns. Most often, the designers use commercial full-wave solvers, which allow for the flexibility to investigate different geometries. However, general-purpose commercial solvers suffer from computation overhead and long simulation times. For these reasons, high-frequency techniques, such as Physical Optics (PO), have played a major role in easing the analysis of quasi-optical systems.

Recently, small-size lens antennas have gained popularity due to their employment flexibility and scanning performance. These have been used as elements for coherent arrays [12] or as the core in the core-shell lens [13]. In these cases, the ray tracing via the Geometrical Optics (GO) or the PO integrals becomes inaccurate because the curvature of the surfaces is small with respect to the wavelength. These limitations call for developing techniques that allow for efficient analysis without compromising accuracy.

For these reasons, the Volumetric Method of Moments explained in Chapter 1 has been developed to study dielectric lenses. A discretization of at most $\lambda_d/10$ is required to analyze lenses with dimensions in the order of a few wavelengths, where $\lambda_d = \lambda_0/\sqrt{\varepsilon_r}$,

λ_0 is the free space wavelength and ε_r the relative dielectric permittivity. For instance, to simulate a lens having a leading dimension of $2\lambda_0 \approx 3\lambda_d$ with a fixed step of $\lambda_d/10$ $N_{\mathrm{MoM}} \approx 3 \times [3\lambda_d/(\lambda_d/10)]^3 \approx 10^5$ unknowns are required. However, the majority of the lens feeds are characterized by dimensions that are much smaller than $\lambda_d/10$. Specifically, depending on the technology, the characteristic dimensions of the dipoles and transmission lines can be micrometric or even nanometric. As a case in integrated technology, the metal thickness is $\approx 0.2 - 2\ \mu\mathrm{m}$, while the width $\approx 1 - 10\ \mu\mathrm{m}$.
Consequently, if one had to use a $10\mu\mathrm{m}$ resolution for a lens with a leading dimension of $2\mathrm{mm}$, the number of unknowns would be $N_{\mathrm{MoM}} \approx 24 \cdot 10^9$. Problems of such scale are not expected to be solved efficiently shortly. To circumvent this problem, a strategy to decouple the analysis of the feed from the lens is developed. To simulate a dielectric lens together with its feed [see Fig. 3.1(a)], this latter, characterized by fine details, can be replaced by an auxiliary one that maintains the same dynamic (i.e., radiating currents), but has a much coarser representation [see Fig. 3.1(b)]. The analysis of the auxiliary feed can be easily performed together with the lens [see Fig. 3.1(c)], for which a coarse discretization suffices. The interaction between the lens and the feed occurs only via the dynamic spectral components. As these have been synthesized to be equivalent for the original and auxiliary dipole, the two problems share the same interaction with the lens.
Correspondingly, the impedance in the presence of the lens can be expressed as the sum of the contribution due to the feed operating without reflections and the one due to the reflections from the lens. These can be extracted from the auxiliary dipole simulation and can then be complemented with the impedance of the finely discretized feed to obtain its original input impedance. This concept is independent of the specific numerical technique used. It finds its largest benefit when structured meshes are employed, but it can also be applied for unstructured mesh when a large imbalance between the feed size and its surroundings is present.
This Chapter is organized as follows. In Section 3.2, the input impedance of the lens antenna is represented with an equivalent circuit where three different contributions are highlighted: the reactive effects, the feed radiation in absence of the lens and the reflection from the lens surface. In Section 3.3, it is explained how the reflection from the lens surface can be estimated by replacing the original feed with an auxiliary one with the same radiation characteristics. Finally, in Section 3.4, this method is validated with a dipole-fed lens antenna and with a double-dipole-fed lens antenna by showing the input impedances and radiation patterns.

3.2 Equivalent Circuit of a Dipole Illuminating a Dielectric Lens

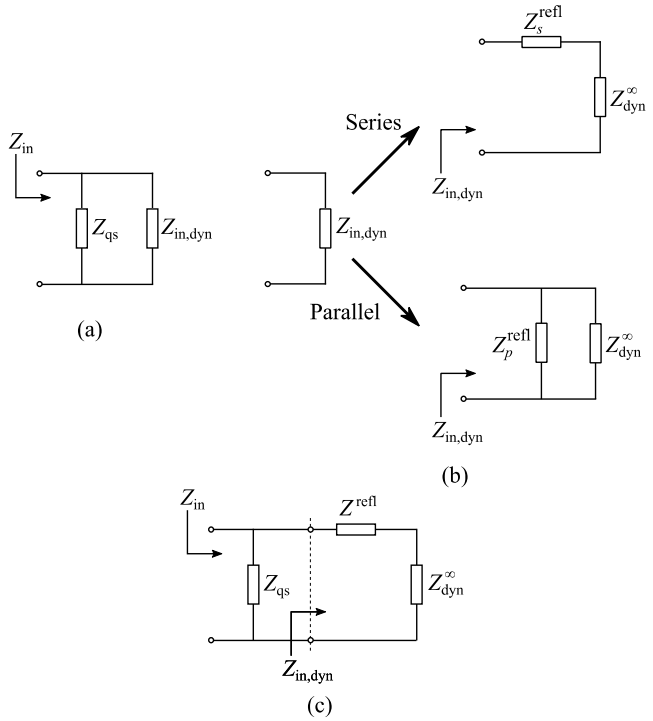

Fig. 3.2. Equivalent circuit representation of the (a) input impedance Z_{in} in terms of the dynamic $Z_{\mathrm{in,dyn}}$ and quasi-static Z_{qs} component, (b) dynamic component $Z_{\mathrm{in,dyn}}$ with the reflections added in series or in parallel to the dynamic component calculated without the reflections $Z_{\mathrm{dyn}}^{\infty}$, and (c) input impedance Z_{in} calculated with the auxiliary sources method.

3.2.1 Dynamic and Quasi-static Components

As shown in Fig. 3.2(a), the input impedance Z_{in} of a dipole can be approximated as the parallel between the quasi-static component Z_{qs}, associated with the capacitance of the gap and the dynamic impedance Z_{dyn}, associated with a wave propagating on the dipole and causing the radiation [6]. In the spectral domain, Z_{dyn} corresponds to the low part of the spectrum, which is dominated by a pole, while Z_{qs} is associated with the high part of the plane-wave spectrum.

3.2.2 The Reflection Component of the Input Impedance

Any input impedance of an antenna is defined as the ratio between integrals on the input ports of the electric field and the magnetic field when one of the two fields is assumed to be the excitation and the other is the unknown of the problem. If a dielectric body is present, a fraction of the radiated fields are reflected by the dielectric-air interface back to the feeding ports, changing the impedance (or the admittance) with respect to the case without the reflections. As the reflections are due to radiative phenomena, these are associated with the dynamic component of the impedance (or the admittance). As the antenna input port can be arbitrarily represented with a series or parallel equivalent circuit [see Fig. 3.2(b)], the correction due to the reflections can be added to the dynamic component calculated in the absence of the reflections. Consequently, the dynamic component of the input impedance or admittance can be expressed as follows

$$Z_{\mathrm{in,dyn}} = Z_{\mathrm{dyn}}^{\infty} + Z_{\mathrm{s}}^{\mathrm{refl}} \tag{3.1}$$

$$Y_{\text{in,dyn}} = Y_{\text{dyn}}^{\infty} + Y_{\text{p}}^{\text{refl}} \tag{3.2}$$

where Z_{dyn}^{∞} and Y_{dyn}^{∞} are the dynamic components of the impedance and the admittance, respectively, calculated without the reflections and $Z_{\text{s}}^{\text{refl}}$ and $Y_{\text{p}}^{\text{refl}}$ are the impedance and admittance, respectively, associated with the reflections. It is worth mentioning that the values of the impedances added in series or parallel are generally different (i.e., $Y_{\text{p}}^{\text{refl}} \neq 1/Z_{\text{s}}^{\text{refl}}$). As in the following, we intend to work with impedances, and for the sake of simplicity, we always refer to the series model (3.1). Because of this, to avoid a redundant notation, the subscript "s" is, from now on, omitted.

All the quantities required for the evaluation of the impedances are calculated at the point r located in the gap, starting from sources located at r' always located on the dipole. The field in the absence of the reflections, i.e., the one associated with Z^{∞}, is evaluated in the near field of the dipole, and it has a fast space variability being calculated with a Green's function $\propto |r - r'|^{-3}$ [see Fig. 3.3(a)]. On the contrary, if the boundaries of the dielectric are sufficiently distant from the dipole, the field associated with the reflections is much less rapidly varying as the field propagates from the dipole to the boundaries and backward, with a pathlength D [see Fig. 3.3(b)]. Therefore, the Green's function of the reflections is dominated by the $|r - r' + D|^{-1}$ term. Due to its fast space variability, the impedance calculated without the reflections highly depends on the specific geometry. In contrast, the impedance associated with the reflections depends mainly on the dynamic component of the currents and not on the particular shape.

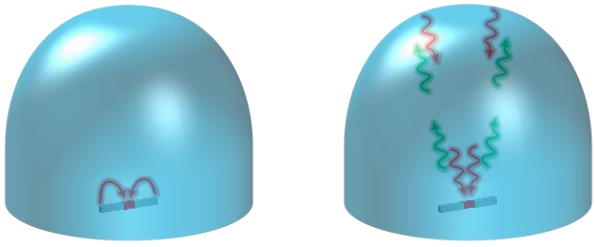

(a) (b)

Fig. 3.3. Sketch of a dipole radiating inside a lens, highlighting (a) the near field component and (b) the waves reflected by the discontinuities to the feed.

3.3 Input Impedance with the Auxiliary Sources Method

3.3.1 Synthesis of the Auxiliary Dipole

Instead of simulating the dipole feeding the lens directly, one can synthesize an *auxiliary dipole*, characterized by a discretization much larger than the original one but which equally radiates without the reflections. This is expressed by the following condition

$$\text{Re}\{Z_{\text{aux}}^{\infty}\} \approx \text{Re}\{Z_{\text{dyn}}^{\infty}\} \tag{3.3}$$

where Z_{aux}^{∞} is the dynamic component of the auxiliary dipole without the reflections. The auxiliary dipole has a discretization much larger than the original one, which implies a much larger feeding gap. Consequently, its quasi-static component is negligible. The

synthesis (3.3) is imposed only on the dynamic part of the impedance as the far-field radiation is independent of the quasi-static part Z_{qs}, which can be added to the auxiliary dipole in post-processing. The advantage of having extracted the quasi-static component is that it makes the simulation of the dipole with a coarse discretization independent of the feeding gap, which would require a high level of detail. Following (3.3), the dynamic impedance of the original dipole can be expressed as follows

$$Z_{\mathrm{dyn}}^{\infty} \approx \mathrm{Re}\{Z_{\mathrm{aux}}^{\infty}\} + jX_{\mathrm{diff}} \tag{3.4}$$

where X_{diff} is defined as follows

$$X_{\mathrm{diff}} = \mathrm{Im}\{Z_{\mathrm{dyn}}^{\infty}\} - \mathrm{Im}\{Z_{\mathrm{aux}}^{\infty}\}. \tag{3.5}$$

Thanks to the coarse mesh, the dipole with the finite dielectric can be simulated, and the input impedance, according to (3.1), can be split as follows

$$Z_{\mathrm{aux}} = Z_{\mathrm{aux}}^{\infty} + Z_{\mathrm{aux}}^{\mathrm{refl}} \tag{3.6}$$

and using (3.4) in (3.6) follows that

$$Z_{\mathrm{aux}} = Z_{\mathrm{dyn}}^{\infty} + Z_{\mathrm{aux}}^{\mathrm{refl}} - jX_{\mathrm{diff}}. \tag{3.7}$$

3.3.2 Estimation of the Reflections

By comparing (3.4) with (3.7), the input impedance of the original dipole in the finite problem can be equal to the one of the auxiliary dipole only if

$$Z_{\mathrm{aux}}^{\mathrm{refl}} \approx Z^{\mathrm{refl}}. \tag{3.8}$$

Since the two dipoles radiate equivalently, this is a reasonable assumption as the reflections are a slow-varying term associated with a long propagation path, and these can be extracted from (3.6) as follows

$$Z_{\mathrm{aux}}^{\mathrm{refl}} = Z_{\mathrm{in,aux}} - Z_{\mathrm{aux}}^{\infty}. \tag{3.9}$$

Then, the dynamic input impedance of the original dipole in the finite medium can be estimated as follows

$$Z_{\mathrm{in,dyn}} \approx Z_{\mathrm{dyn}}^{\infty} + Z_{\mathrm{aux}}^{\mathrm{refl}} \tag{3.10}$$

Finally, the input impedance can be obtained by adding Z_{qs} in parallel

$$Z_{\mathrm{in}} = Z_{\mathrm{in,dyn}} \parallel Z_{\mathrm{qs}}. \tag{3.11}$$

$Z_{\mathrm{dyn}}^{\infty}$ is calculated with the extraction of Z_{qs} from the input impedance of the original dipole radiating in the absence of the reflections. There are no constraints on the methods used to derive this latter, which can be evaluated with a commercial solver, a spectral domain

representation, or with the V-MoM used to extract the reflections. The final steps (3.10) and (3.11) can be represented by the equivalent circuit in Fig. 3.2(c).

3.4 Results

3.4.1 Single Dipole

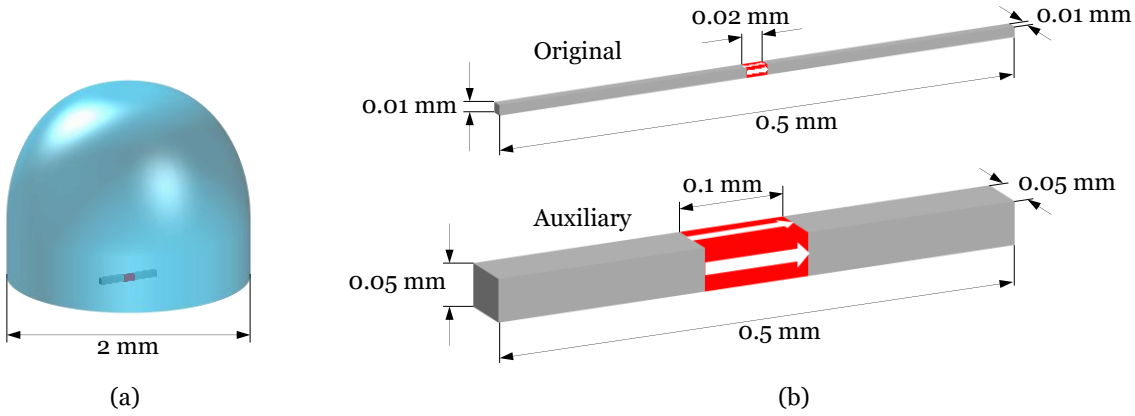

Fig. 3.4. (a) Sketch of the dipole fed lens, (b) details of the original and auxiliary dipole.

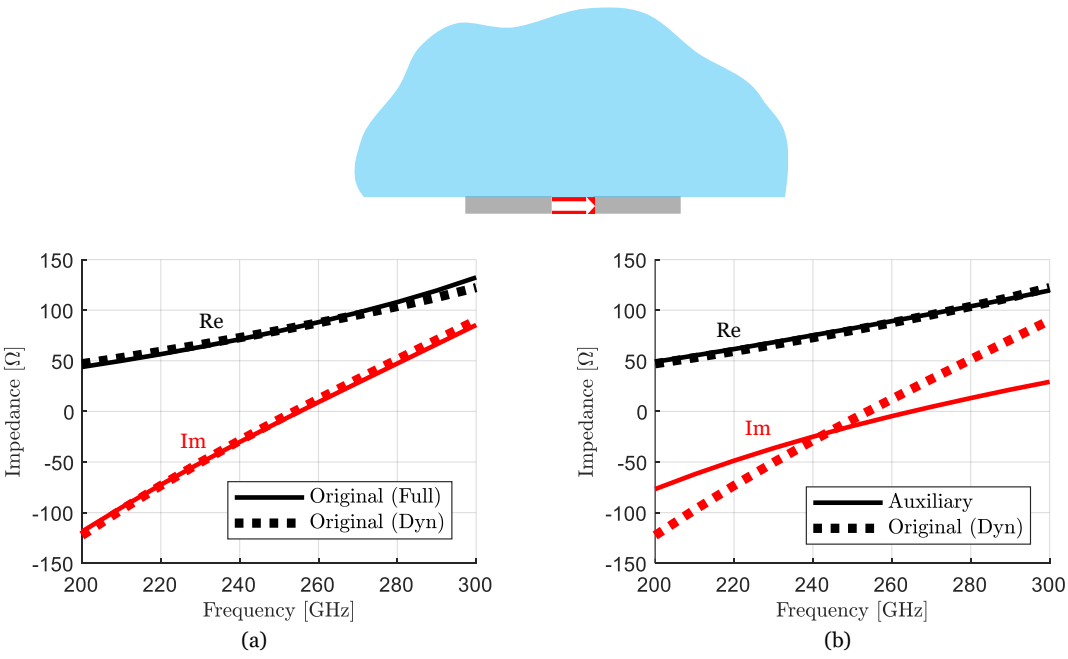

Fig. 3.5. Input impedance calculated without the reflections for (a) the original dipole, and (b) the auxiliary dipole compared with the dynamic component of the original one.

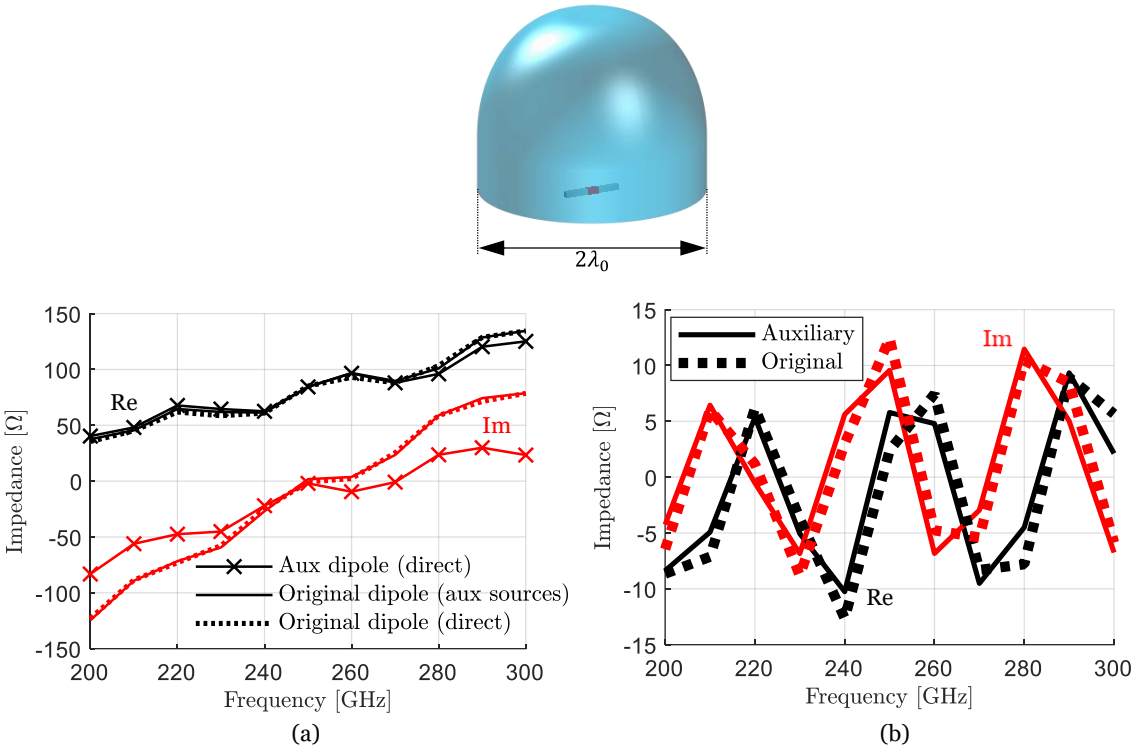

Fig. 3.6. (a) Input impedance of the dipole fed lens calculated via direct simulation and with the auxiliary sources method, and (b) reflections extracted with the direct simulation and the auxiliary problem.

We aim to simulate with the V-MoM explained in Chapter 2 a dipole long $\ell = 0.5$ mm placed on the focus of an elliptical lens with a diameter 2 mm and dielectric permittivity $\varepsilon_r = 2.34$. The dipole has a square cross-section with a side $w_y = w_z = 0.010$ mm, and it is fed by a Δ-gap generator $\Delta = 0.02$ mm long, as shown in Fig. 3.4. A structured mesh would require a discretization of at least 0.010 mm, i.e., the side of the cross-section, yielding 16×10^6 unknowns. With the proposed method, it is possible to use the volumetric method of moments and a structured mesh and achieve comparable results by using an auxiliary dipole 0.05 mm (see Fig. 3.4), and 141×10^3 unknowns.

The original dipole is first simulated with the method of moments when radiating at the interface between free space and an infinite homogeneous medium with permittivity $\varepsilon_r = 2.34$, and its impedance in the absence of reflections is calculated. This condition is realized with the V-MoM, by adding a matching layer over the dielectric. The quasi-static impedance Z_{qs} is then isolated, and the dynamic component Z_{dyn} is shown in Fig. 3.5(a), where it is compared with the total input impedance. Then, the auxiliary dipole is synthesized with the V-MoM, and its impedance is shown in Fig. 3.5(b). The auxiliary dipole radiating into the lens is efficiently simulated, thanks to the coarse discretization. The corresponding input impedance and the reflections extracted with (3.9) are shown in Fig. 3.6(a) and (b), respectively. Finally, the input impedance of the original dipole is estimated with (3.11), and its values are shown in Fig. 3.6(a), and compared with the direct simulation, which is possible to calculate due to the relatively small size of the problem. In Fig. 3.6(b), the reflections from the lens extracted with the original dipole are compared with those extracted with the auxiliary one, verifying that the specific geometry of the feed does not affect the interaction with the lens if the auxiliary and original dipole equivalently radiate in the far field.

In Fig. 3.7(a), the directivity patterns of the auxiliary and original problems are compared on the E- and H-planes.

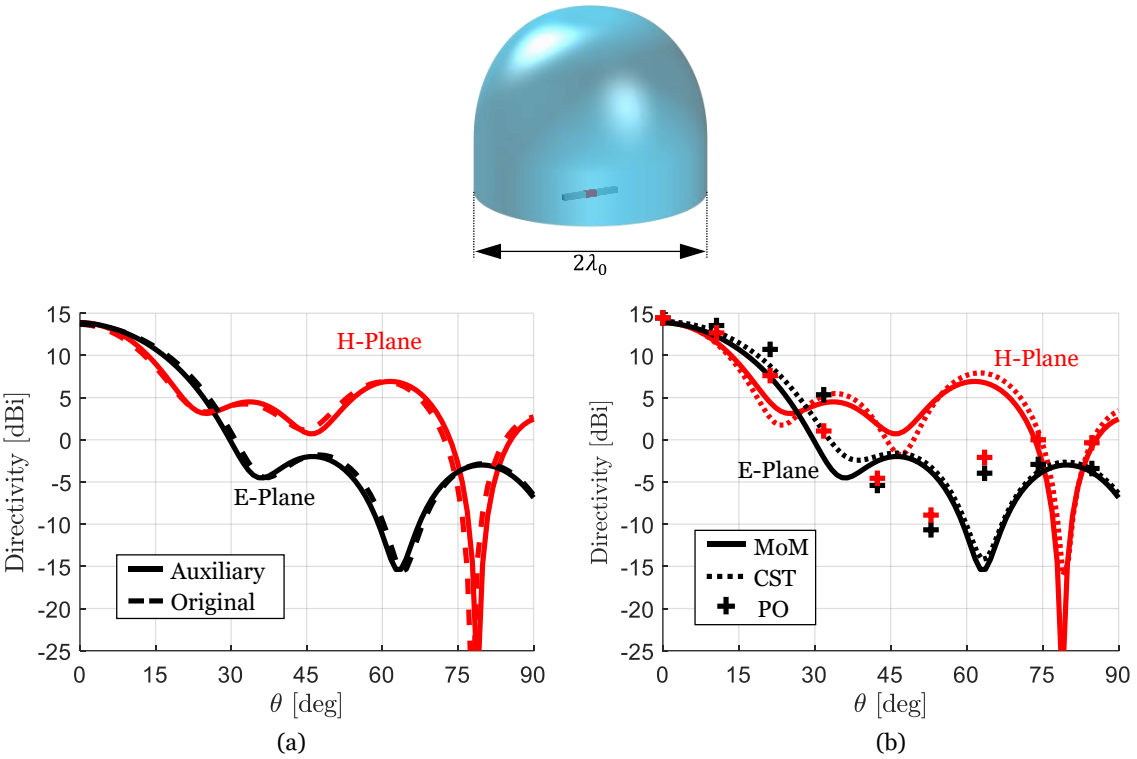

Fig. 3.7. Directivity on the E- and the H-plane at 250 GHz for the dipole-fed lens (a) calculated with the MoM for the original and the auxiliary problem, and (b) calculated with CST, the PO, and the MoM (auxiliary).

Due to the condition (3.3) and the fact that the details of the feed do not affect the far field, the original and auxiliary dipoles have the same pattern. In Fig. 3.7(b), the directivity patterns of the lens fed by the auxiliary dipole are shown at 250 GHz, and the values obtained with the proposed method are compared with CST and the Physical Optics (PO) [15]. As the PO fields have been calculated for $\theta \in [0°, 90°]$, to obtain an objective comparison of the directivity, the normalization for the method of moments and CST is done with respect to the power radiated in the upper hemisphere only. The patterns obtained by the proposed method are validated with CST. The patterns also highlight the inaccuracy of the PO for the study of small lens antennas.

To show the validity of this procedure for off-focus dipoles, the feed of the previous geometry is shifted by 0.75 mm on the H-plane, i.e., an extreme configuration with the dipole still entirely underneath the lens, as shown in Fig. 3.8(a). As the synthesis does not depend on the geometry of the surrounding dielectric, the synthesized auxiliary dipole is the one of Fig. 3.5(b). The input impedance is compared in Fig. 3.8(b) with the standard simulation of the dipole displaced under the lens, showing an excellent agreement due to the accurate extraction of the reflections Fig. 3.8(c). The patterns on the H-plane at 250 GHz are shown in Fig. 3.8(d), where the directivity calculated with this method is compared with CST and the PO. As before, the directivity is calculated by considering only the power radiated in the upper hemisphere. Despite the scanning configuration, the directivity results are higher than at broadside because of a lower radiated power in the upper hemisphere due to the scanning. While the patterns calculated with the auxiliary sources maintain a good accuracy also in off-focus configurations, the PO commits larger errors.

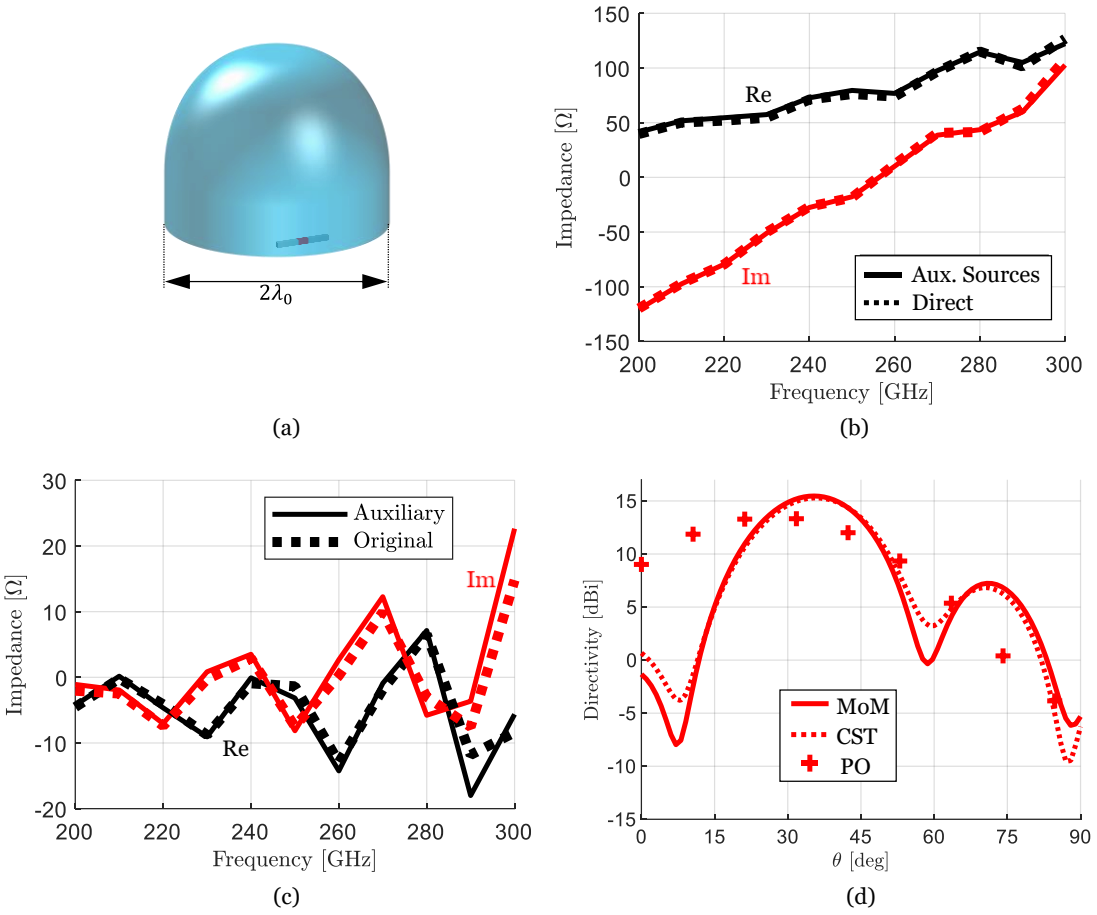

Fig. 3.8. (a) Geometry of the off-focus dipole, shifted by 0.75 mm in the H-Plane, (b) Input impedance of the dipole fed lens calculated via direct simulation and with the auxiliary sources method, (b) reflections extracted with the direct simulation and the auxiliary problem, and (d) comparison of the directivity patterns on the H-plane at 250 GHz with an off-focus offset 0.75 mm.

3.4.2 Double Dipole

The procedure can be extended to the analysis of a double-dipole fed lens, as shown in Fig. 3.9(a)

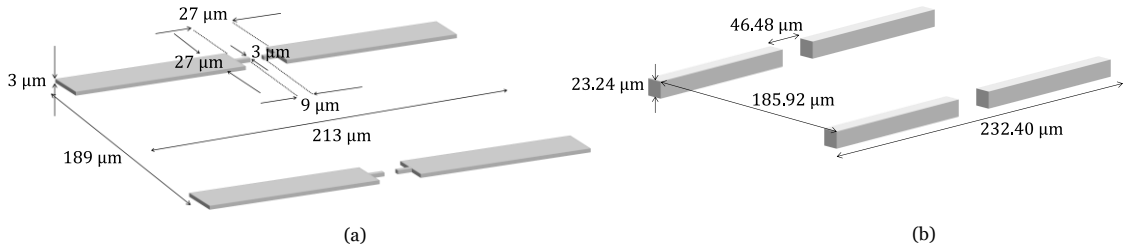

Fig. 3.9. Sketch of (a) the original and (b) the auxiliary double dipole.

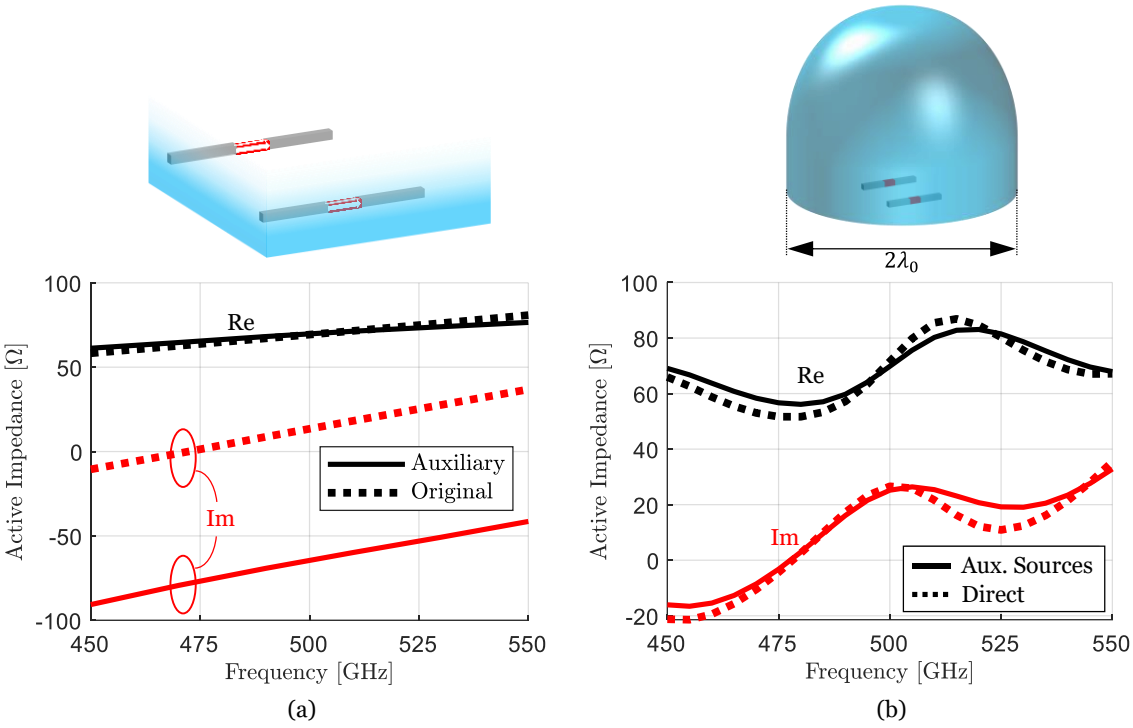

Fig. 3.10. Active impedance of the original and auxiliary double dipole (a) without the reflections and (b) with the dielectric lens.

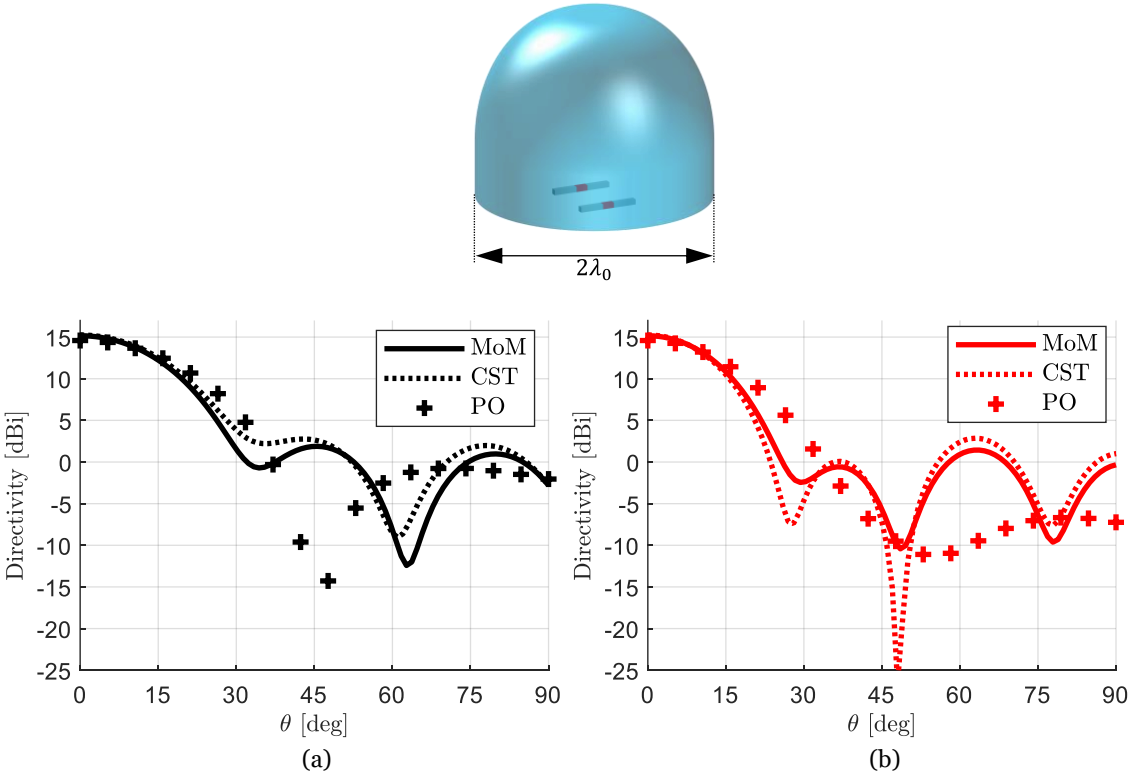

Fig. 3.11. Patterns at 500 GHz (a) in the E- and (b) the H-plane calculated with the MoM (auxiliary), CST, and the PO.

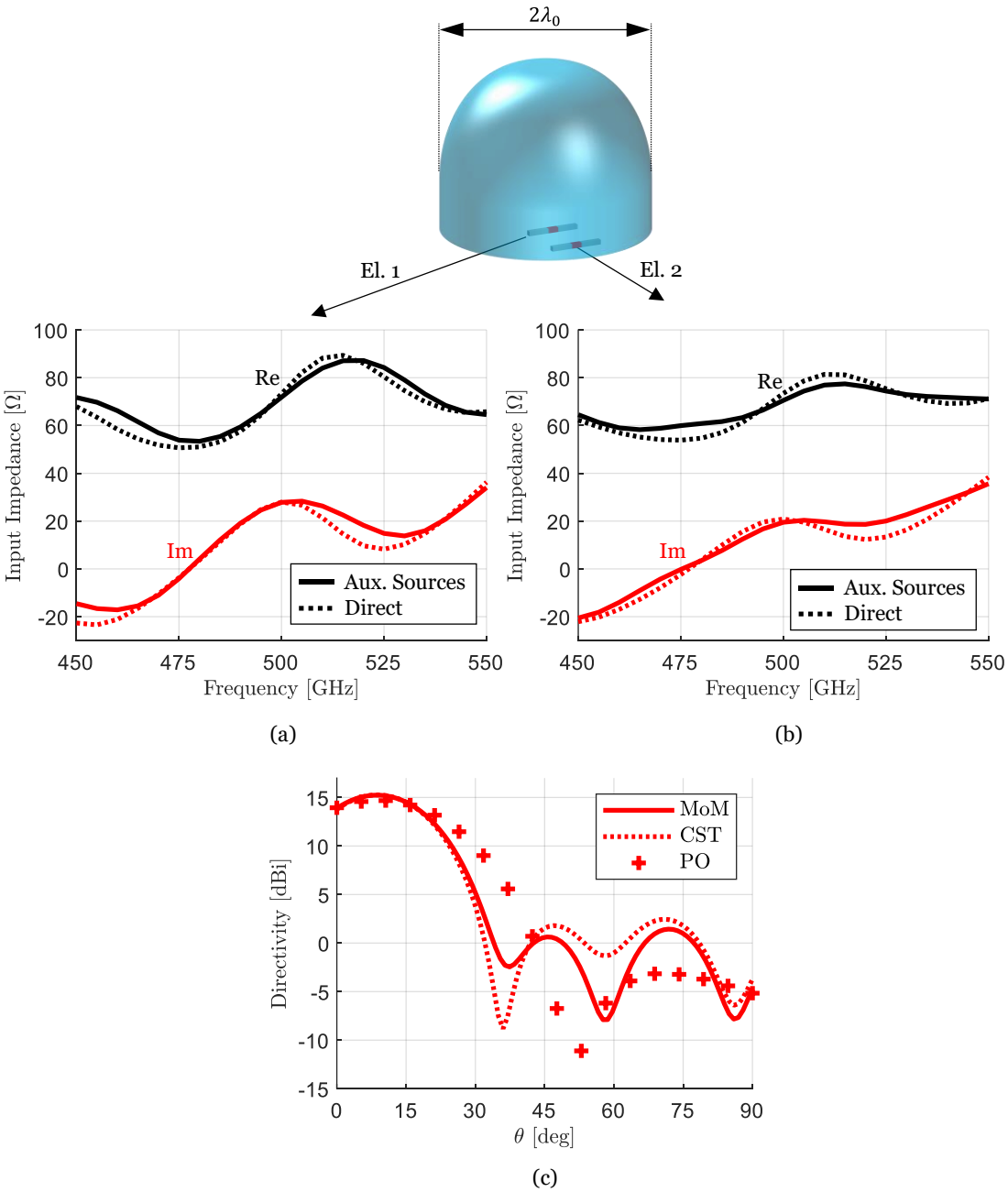

Fig. 3.12. Active impedance of element (a) 1, (b) 2, and (c) directivity patterns on the H-plane at 500 GHz calculated with the V-MoM (auxiliary), CST, and the PO.

In this case, the synthesis of the auxiliary feed is carried out on the active impedances, i.e., the impedances when both dipoles are excited. The original double-dipole radiating in the semi-infinite medium is obtained with a CST simulation, as the level of detail implies a computational burden that is too heavy for the V-MoM. The quasi-static component is extracted from a single dipole as it is only due to the capacitive effects around the gap, which does impact the mutual coupling between the dipoles.

The two auxiliary dipoles in an array configuration are synthesized with the V-MoM, where the side of each dipole is 0.023 mm, the length is 0.230 mm, the gap is 0.046 mm long, and the spacing is 0.184 mm, as shown in Fig. 3.9(b). The comparison between the input impedance of the real and auxiliary dipoles is shown in Fig. 3.10(a). The input

impedance calculated with the auxiliary sources is compared with the direct CST simulation in Fig. 3.10(b), showing a good agreement.

	$D = 1\text{mm}$	$D = 2.5\text{mm}$
V-MoM	5s	677 sec
CST	72s	311 sec

Table 3. Computational time of CST and the V-MoM to calculate the active input impedance at 300GHz of the double dipole for different lens diameter in the on-focus case. CPU: Intel® Core™ i5-12500 3.00GHz, RAM: 16GB

This example shows that the auxiliary sources method can also be extended to the analysis of realistic feeds. Moreover, it also proves the strength and flexibility of the method, as it shows that the simulation of any radiator close to a dielectric body can be simplified by separating the feed from the interaction with the body, where these two contributions can be simulated with different techniques.
Fig 3.12 shows the active input impedances of the two elements and the pattern of the lens antenna at 500GHz when the array is shifted by 0.139 mm from the focus. In the off-focus case, due to the asymmetry of the problem, two simulations must be carried out with the V-MoM to calculate the active impedances. However, this is not a limiting factor, as the time required by a single V-MoM simulation is much less than CST.

To test the potential of this method, the same feed of Fig. 3.9 and Fig. 3.10(a) is used to illuminate a larger lens with a diameter of 2.5 mm. The results in terms of the input impedance and the patterns are shown in Fig. 3.13 for the double dipole placed in the focus and in Fig. 3.14 for the dipole shifted by 0.139 mm from the focus. Table 3 shows the comparison in terms of computational time between the V-MoM and CST. While the V-MoM outperforms CST for $D = 1\,\text{mm}$, when the number of unknowns is 173862, the increase of the unknowns for $D = 2.5\,\text{mm}$ (2621946 unknowns) affects the computational speed excessively. Therefore, this calls for the use of a preconditioner to stabilize the number of iterations with respect to the geometry.

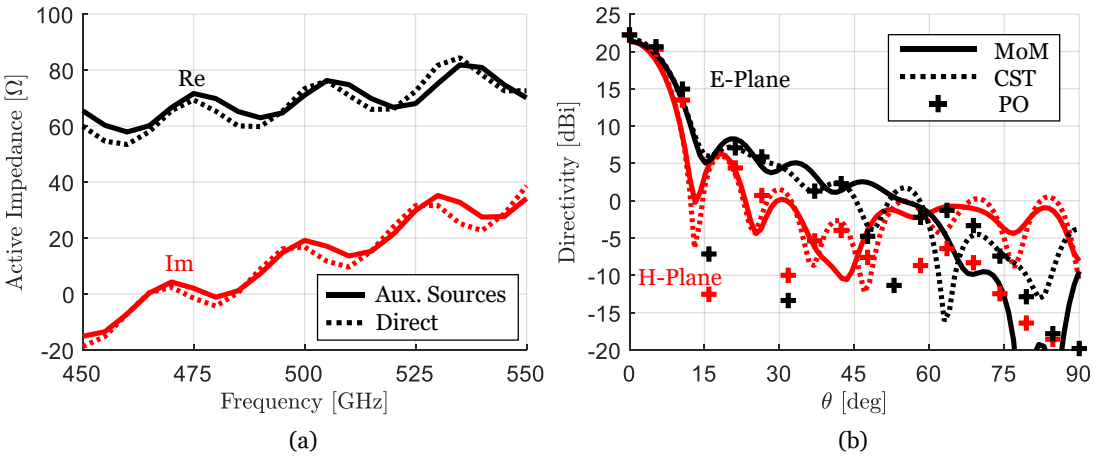

Fig. 3.13. (a) Active impedance calculated with the auxiliary sources method and with direct simulation (CST) and (b) directivity patterns in the E- and H-plane at 500 GHz calculated with the V-MoM (auxiliary), CST, and the PO.

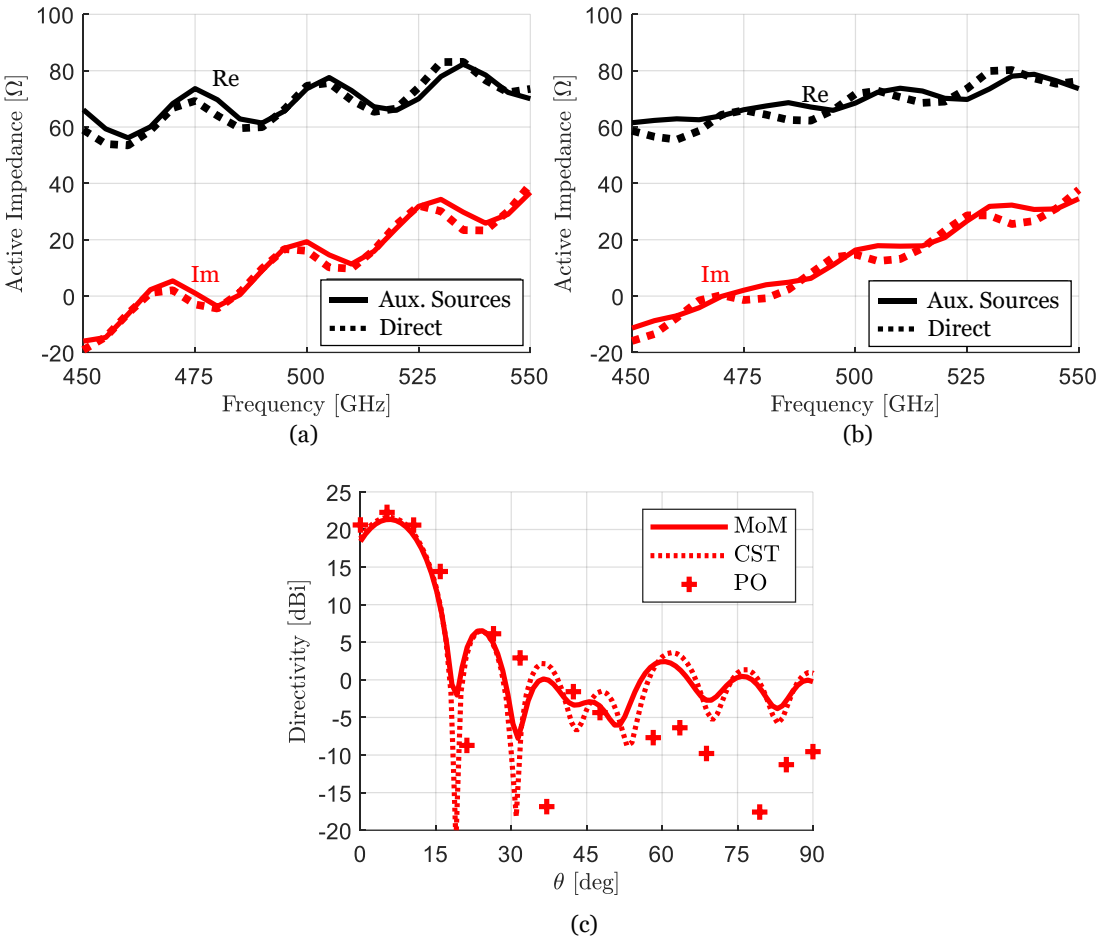

Fig. 3.14. Active impedance of element (a) 1, (b) 2, and (c) directivity patterns on the H-plane at 500 GHz calculated with the V-MoM (auxiliary), CST, and the PO.

4 Layered Media Analysis of Lossy and Non-zero Thickness Metal Dipole

In this Chapter, we will introduce a novel method to study the current distribution on a dipole embedded in a layered media when excited by a δ-gap generator. This method starts from the Green's Function of an infinite dipole presented in [6] where, differently from the previous analysis [16], the thickness of the conductor is also considered. Then, similarly to what has been done for the slots in [17], the field located on the termination of the dipole is included to take into account the fitness of the geometry. In Chapter 3, it was explained that, to synthetize the equivalent dipole with the V-MoM, the input impedance of the original dipole radiating in the absence of the reflections is needed. This latter can be found with a full wave solver such as CST, but the time required for the simulation becomes significant for dipoles with dimensions much smaller than the wavelength. Therefore, the method proposed in this Chapter aims to replace the full-wave simulation with a faster and more flexible analytical formulation.
Moreover, this formulation gives insight into the different spectral components of the currents by distinguishing the ones responsible for radiation and the ones for reactive effects. The Chapter is structured as follows. In Section 4.1, a background on the Green's function for the infinite dipole is provided. Next, in Section 4.2. the formulation for the finite dipole is explained. Finally, Section 4.3 consists of a validation, where the input impedances and current distributions of dipoles with different geometries calculated with our method and with CST are compared.

4.1 Background on the Dipole Green's Function

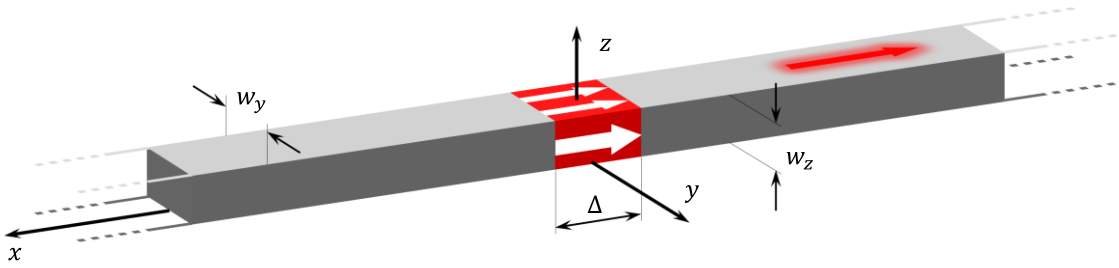

Fig. 4.1. Illustration of an infinite dipole oriented along x, w_y wide and w_z thick, and excited by a δ-gap generator Δ long.

In this section, the theoretical background of the Dipole Green's Function, which is necessary to understand the formulation of the current distribution of a finite dipole, is provided. Let us consider an infinite dipole embedded in an arbitrary stratification, oriented along the x-axis as shown in Fig. 4.1. The dipole is made of a homogenous

material with a resistivity ρ, a rectangular cross-section A, w_y wide and w_z thick and fed by Δ-gap generator of length Δ where the field is assumed to be uniform.
Let us start with Ohm's Law, which is as follows

$$\vec{j} = \frac{1}{\rho}\vec{e} = \frac{1}{\rho}\left(\vec{e}^{\,i} + \vec{e}^{\,s}\right) \tag{4.1}$$

where the total field $\vec{e}$ is expressed as the sum of the incident and the scattered field $\vec{e}^{\,i}$ and $\vec{e}^{\,s}$, respectively. Only the x- component of the current is considered due to the elongated geometry. Due to the rectangular cross-section, the separation of variables can be applied, and (4.1) can be rewritten as follows

$$\rho i(x) j_t(y,z) = v(x) e_t^i(y,z) + e_x^s(x,y,z) \tag{4.2}$$

where $i(x)$ and $j_t(x)$ are the longitudinal and transverse currents distributions, $v(x)$ and $e_t^i(y,z)$ are the longitudinal and transverse components of the incident field, and $e_x^s(x,y,z)$ is the x-component of the scattered field. As the incident field is modelled as a Δ-gap generator, it can be written as follows

$$v(x) = \frac{V_0}{\Delta}\,\mathrm{rect}\left(\frac{x}{\Delta}\right) \tag{4.3}$$

$$e_t^i(y,z) = \mathrm{rect}\left(\frac{y}{w_y}\right)\mathrm{rect}\left(\frac{z}{w_z}\right) \tag{4.4}$$

where $\mathrm{rect}(x)$ is defined as follows

$$\mathrm{rect}(x) = \begin{cases} 1 & \text{if } |x| < 0.5 \\ 0.5 & \text{if } |x| = 0.5 \\ 0 & \text{if } |x| > 0.5 \end{cases} \tag{4.5}$$

and V_0/Δ is the magnitude of the incident field on the gap. By substituting (4.3) and (4.4) in (4.2) and by expressing the scattered field as the convolution between the stratified media Green's function and the currents, (4.2) becomes as follows

$$\frac{V_0}{\Delta}\mathrm{rect}\left(\frac{x}{\Delta}\right) e_t^i(y,z) = \rho i(x) j_t(y,z) - \int_{-\infty}^{+\infty} \int_{-\frac{w_y}{2}}^{\frac{w_y}{2}} \int_{0}^{w_z} g_{xx}^{EJ}(x-x', y-y', z-z') i(x') j_t(y',z') dx' dy' dz'. \tag{4.6}$$

Next, $g_{xx}^{EJ}(x-x', y-y', z-z')$ can be written as the inverse Fourier transform of the spectral domain stratified media Green's function as follows

$$g_{xx}^{EJ}(x-x', y-y', z-z') = \frac{1}{4\pi^2} \int_{-\infty}^{+\infty} \int_{-\infty}^{+\infty} G_{xx}^{EJ}\left(k_x, k_y, z, z'\right) e^{-jk_x(x-x')} e^{-jk_y(y-y')}\, dk_x dk_y \tag{4.7}$$

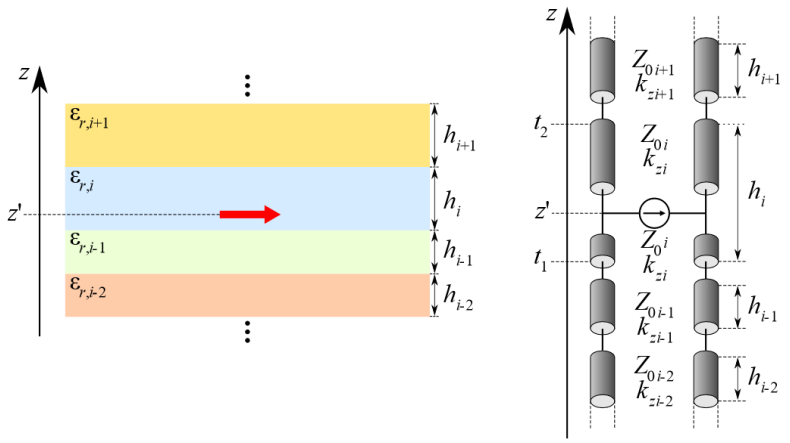

(a) (b)

Fig. 4.2. (a) Vertical section of a dipole embedded in an arbitrary stratification and (b) transmission line equivalent representation of the stackup

where $G_{xx}^{EJ}(k_x, k_y, z, z')$ has the following analytical expression

$$G_{xx}^{EJ}(k_x, k_y, z, z') = \frac{v_{\mathrm{TM}}(z, z')k_x^2 + v_{\mathrm{TE}}(z, z')k_y^2}{k_x^2 + k_y^2} \tag{4.8}$$

where $v_{\mathrm{TM}}(z, z')$ and $v_{\mathrm{TE}}(z, z')$ are the voltage solutions at z of the TE and TM equivalent transmission lines problems when the source is located at z', as illustrated in Fig. 4.2. Thanks to the rectangular cross-section, one can assume that the separation of variables can be applied to the transverse current distribution $j_t(y, z)$ which becomes as follows

$$j_t(y, z) = j_{t,y}(y) j_{t,z}(z). \tag{4.9}$$

By substituting (4.7) and (4.9) in (4.6), one obtains the following equation

$$\begin{aligned}\frac{V_0}{\Delta}\mathrm{rect}\left(\frac{x}{\Delta}\right)e_t^i(y,z) = \rho i(x) j_t(y,z) \\ -\int_{-\infty}^{+\infty}\int_{-\frac{w_y}{2}}^{\frac{w_y}{2}}\int_{0}^{w_z}\left[\frac{1}{4\pi^2}\left(\int_{-\infty}^{+\infty}\int_{-\infty}^{+\infty} G_{xx}^{EJ}(k_x,k_y,z,z')e^{-jk_x(x-x')}e^{-jk_y(y-y')}\,dk_x dk_y\right)\right. \\ \left.\times\, i(x')j_{t,y}(y')j_{t,z}(z')\right]dz'dy'dx'.\end{aligned} \tag{4.10}$$

The integral in x' and in y' can be closed into the Fourier transform of $i(x')$ and $j_{t,y}(y')$ as follows

$$\begin{aligned}\frac{V_0}{\Delta}\mathrm{rect}\left(\frac{x}{\Delta}\right)e_t^i(y,z) = \rho i(x) j_t(y,z) \\ -\frac{1}{4\pi^2}\int_{0}^{w_z}\int_{-\infty}^{+\infty}\int_{-\infty}^{+\infty} G_{xx}^{EJ}(k_x,k_y,z,z')I(k_x)J_{t,y}(k_y)j_{t,z}(z')e^{-jk_x x}e^{-jk_y y}dk_x dk_y dz'.\end{aligned} \tag{4.11}$$

The longitudinal incident field and the longitudinal current distribution can be written with their inverse Fourier transform and (4.11) becomes as follows

$$\int_{-\infty}^{+\infty} V_0 \mathrm{sinc}\left(\frac{k_x \Delta}{2}\right) e_t^i(y,z) e^{-jk_x x} dk_x$$
$$= \rho \int_{-\infty}^{+\infty} I(k_x)\, j_t(y,z) e^{-jk_x x} dk_x - \frac{1}{2\pi} \int_0^{w_z} \int_{-\infty}^{+\infty} \int_{-\infty}^{+\infty} \left[G_{xx}^{EJ}(k_x, k_y, z, z')\, I(k_x) \right.$$
$$\left. \times J_{t,y}(k_y) j_{t,z}(z') e^{-jk_x x} e^{-jk_y y} \right] dk_x dk_y dz'. \quad (4.12)$$

As the dipole is considered to be infinite along x, the equality in (4.12) holds for ever x and the spectra in k_x can be equated

$$V_0 \mathrm{sinc}\left(\frac{k_x \Delta}{2}\right) e_t^i(y,z) = \rho I(k_x) j_t(y,z)$$
$$- \frac{1}{2\pi} \int_0^{w_z} \int_{-\infty}^{+\infty} G_{xx}^{EJ}(k_x, k_y, z, z') I(k_x) J_{t,y}(k_y) j_{t,z}(z') e^{-jk_y y} dk_y dz' \quad (4.13)$$

where $\mathrm{sinc} \coloneqq \sin(x)/x$ is the Fourier transform of the rect function. Then, one can define the following projection operator on the cross-section of the dipole

$$\langle f, g \rangle_A = \iint_A f(y,z) g^*(y,z) dy dz \quad (4.14)$$

to project the left and right-hand side of (4.13) on the test function $\tilde{j}_t$, which is expressed as follows

$$\tilde{j}_t(y,z) = \tilde{j}_{t,y}(y) j_{t,z}(z). \quad (4.15)$$

As the test function is defined to have an unitary integral flux on the cross-section, i.e. $\langle \tilde{j}_t, e_t^i \rangle_A = 1$, after the projection of (4.15) on both sides of (4.13), the Fourier transform of the current I along the dipole can be evaluated as follows

$$I(k_x) = \frac{V_0 \mathrm{sinc}(k_x \Delta/2)}{D(k_x)} \quad (4.16)$$

where $D(k_x)$ is the transverse Green's function of the dipole, defined in the following manner

$$D(k_x) = \rho \langle \tilde{j}_t, j_t \rangle_A - \frac{1}{2\pi} \int_0^{w_z} \int_0^{w_z} \int_{-\infty}^{+\infty} \left[G_{xx}^{EJ}(k_x, k_y, z, z') J_{t,y}(k_y) \tilde{J}_{t,y}(-k_y) \right.$$
$$\left. \times j_{t,z}(z') \tilde{j}_{t,z}^*(z) \right] dk_y dz' dz. \quad (4.17)$$

By taking advantage of the formulation in [18] for $v_{\mathrm{TM}}(z,z')$ and $v_{\mathrm{TE}}(z,z')$ in (4.8) and for suitable choices of j_t and $\tilde{j}_t$ the integrals in z and z' can be closed analytically.

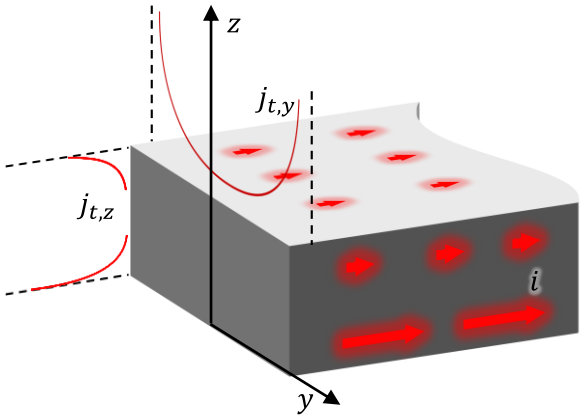

Fig. 4.3. Sketch of the current distributions on the dipole where $j_{t,y}$ is the y-dependent distribution, $j_{t,z}$ are the z-dependent distributions and i is the currents along the x-axis.

The current distribution along y in (4.9) is chosen to have an edge singular behavior

$$j_{t,y}(y) = \frac{2}{\pi w_y} \frac{1}{\sqrt{1-\left(2y/w_y\right)^2}} \mathrm{rect}\left(y/w_y\right) \tag{4.18}$$

And the test function $\tilde{j}_{t,y}(y)$ in (4.15) is as follows

$$\tilde{j}_{t,y}(y) = \frac{1}{w_y} \mathrm{rect}\left(y/w_y\right) \tag{4.19}$$

On the other hand, the choice of $j_{t,z}(z)$ in (4.9) and $\tilde{j}_{t,z}(z)$ in (4.15) must take into account the stratification where the dipole is embedded in, which causes an imbalance between the currents flowing on the top and the one flowing on the bottom. Without going into detail, which can be found in [6], the current distribution $j_{t,y}(z)$ is chosen to be asymmetric with respect the center of the dipole and it is given by the following expression

$$j_{t,z}(z) = \tilde{j}_{t,z}(z) = \frac{(1+j)\left(Re^{-(1+j)z/\delta_p} + e^{(1+j)(z-w_z)/\delta_p}\right)}{2\delta_p(R+1)e^{-(1+j)w_z/\delta_p}\left(e^{(1+j)w_z/\delta_p}-1\right)} \mathrm{rect}\left(\frac{z-w_z/2}{w_z}\right) \tag{4.20}$$

where δ_p is the penetration depth and R is a scalar which takes into account the asymmetries on the current on the top and on the bottom of the dipole. Thanks to this choice of $j_{t,z}(z)$, the current flowing on the dipole is a superposition of the 2 dominant modes of the stratification and it takes into account the difference between the current flowing on top and below the dipole. Fig. 4.3 shows a schematic illustration of the current distributions on the dipole.
Finally, the current distribution in the space domain can be written as the inverse Fourier transform of (4.16) as follows

$$i(x) = \frac{V_0}{2\pi} \int_{-\infty}^{+\infty} \frac{\mathrm{sinc}(k_x\Delta/2)}{D(k_x)} dk_x. \tag{4.21}$$

In the case of a dominant polar contribution, such as in a microstrip or in along dipole, the current spectrum in (4.16) can be approximated with its Laurent series about the pole

k_{xp} whose values is found by solving the dispersion equation $D(k_x) = 0$. This part of the current spectrum constitutes the dynamic component of the current and it is expressed as follows

$$I(k_x) \approx I_{\mathrm{dyn}}(k_x) = \frac{2k_{xp}\mathrm{sinc}\left(\frac{k_x\Delta}{2}\right)}{D'\left(k_{xp}\right)\left(k_x^2 - k_{xp}^2\right)} \quad \text{for } k_x \to k_{xp}. \tag{4.22}$$

By performing the inverse Fourier transform of (4.22), the dynamic component of the current can be written as a travelling wave outside the feeding gap

$$i_{\mathrm{dyn}}(|x| > \Delta/2) = -j\frac{\mathrm{sinc}(k_x\Delta/2)}{D'(k_x)}e^{-jk_{xp}|x|} \tag{4.23}$$

and as a standing wave inside the gap

$$i_{\mathrm{dyn}}(|x| < \Delta/2) = 2\frac{1 - \cos\left(k_{xp}x\right)}{\Delta k_{xp}D'(k_x)}e^{-jk_{xp}\Delta/2}. \tag{4.24}$$

The dynamic part of the current is a good approximation of the total current when it is evaluated away from the gap or for large gap size (i.e. $\Delta > \lambda_0/10$). However, closer to the gap or for small gap size, the high spectrum of the current must be also considered. This latter is associated with the quasi-static component of the current which can be approximated with the following asymptotic expression for $D(k_x)$

$$D(k_x) \approx D_\infty(k_x) = \rho\langle \tilde{j}_t, j_t\rangle_A - \frac{J_{t,y}(0)}{2\pi}\int_0^{w_z}\int_0^{w_z} G_{xx}^{EJ}(k_x, 0, z, z')\, j_{t,z}(z')\tilde{j}_{t,z}^*(z)dz'dz$$

$$\text{for } k_x \to \infty. \tag{4.25}$$

The next step is to define the admittances associated with the dynamic and the quasi-static component of the current. The former can be calculated by extending to the dipoles the procedure presented for the slots in [19]

$$Y_{\mathrm{dyn}} = -\frac{1}{2\pi}\int_{-\infty}^{+\infty}\frac{2k_{xp}\mathrm{sinc}(k_x\Delta/2)}{D'\left(k_{xp}\right)\left(k_x^2 - k_{xp}^2\right)}dk_x \tag{4.26}$$

and the latter is defined by the following expression

$$Y_{\mathrm{qs}} = \frac{1}{2\pi}\int_{-\infty}^{+\infty}\frac{\mathrm{sinc}^2(k_x\Delta/2) - \mathrm{sinc}^2\left(k_x\Delta_{\mathrm{large}}/2\right)}{D_\infty(k_x)}dk_x \tag{4.27}$$

where Δ_{large} is a feeding gap much larger than the original gap Δ, typically in the order of $\lambda_0/10$. The admittance Y_{qs} represents the capacitive effect of the feeding gap. The subtraction of $\mathrm{sinc}^2\left(k_x\Delta_{\mathrm{large}}/2\right)$ aims at removing the lower part of the spectrum while untouching the higher part, which, for large gap size, it is negligible.

4.2 Formulation

4.2.1 The Integral Equation and the Current Spectrum

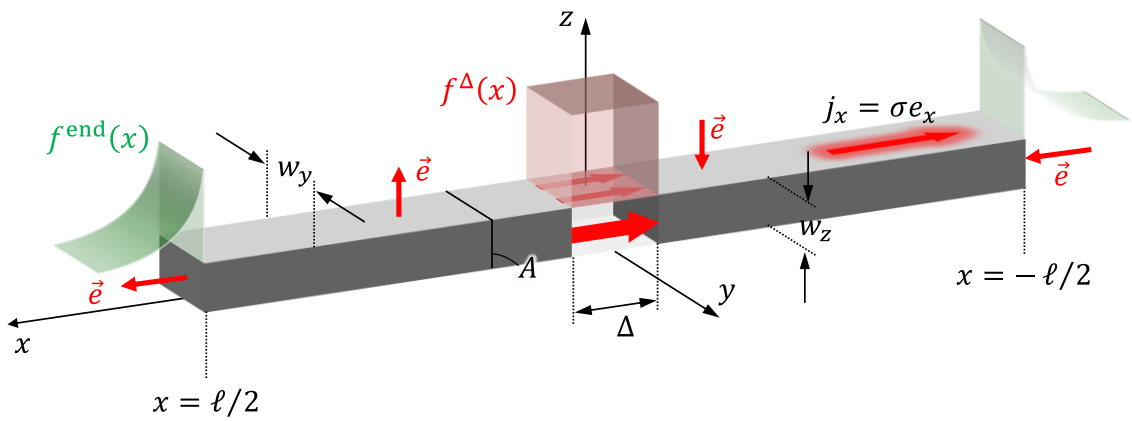

Fig. 4.1. Sketch of a dipole of length ℓ, width w_y, and thickness w_z, and the representation of the longitudinal distributions on the gap and after the endpoints.

Let us consider a dipole oriented along the x-axis, imagined embedded in arbitrary stratified media, and constituted by a material of conductivity σ (or equivalently resistivity $\rho = 1/\sigma$), as shown in Fig. 4.1. It is fed with a voltage V_0 by a Δ-gap generator of length Δ located at the center. The dipole is w_y wide and w_z thick and its length is distributed between $x = -\ell/2$ and $x = \ell/2$. Due to its elongated geometry and the rectangular cross-section, only the x-component of the electric field is considered to be significant, and the separation of variables can be applied. The x-component of the incident field e_x^i can be written as follows

$$e_x^i(x,y,z) = V_0 f^{\Delta}(x) e_t(y,z) \tag{4.28}$$

where f^{Δ} and e_t are the excitation's longitudinal and transverse distributions. The x-component of the total electric field e_x can be expressed by resorting to the local form of Ohm's law as follows

$$e_x(x,y,z) = \rho i(x) j_t(y,z) \chi_{\mathrm{dip}}(x) + V_{\mathrm{end}} f^{\mathrm{end}}(x) e_t(y,z) \tag{4.29}$$

where i is the longitudinal current distribution along the dipole, j_t is the transverse current distribution and χ_{dip} is the characteristic function of the dipole (i.e., $\chi_{\mathrm{dip}} = 1$ for x located in the dipole, and $\chi_{\mathrm{dip}} = 0$ elsewhere). The functions f^{end} and e_t model the longitudinal and transverse field distribution after the dipole's endpoints, as sketched in Fig. 4.1 and V_c is the amplitude at $x = \pm\ell/2$, which is assumed to be the same for either sides, due to the excitation placed in the center of the dipole. The x-component of the scattered field e_x^s can be expressed by the following convolution

$$e_x^s(x,y,z) = g_{xx}^{EJ}(x,y,z) * \left[i(x) \chi_{\mathrm{dip}}(x) j_t(y,z) \right] \tag{4.30}$$

with g_{xx}^{EJ} being the xx-component of the Green's function providing the electric field from the electric currents and $*$ denoting the convolution operator. Finally, by enforcing $e_x = e_x^i + e_x^s$, one can write the following integral equation

$$V_0 f^{\Delta}(x) e_t(y,z) - V_{\text{end}} f^{\text{end}}(x) e_t(y,z) = \left(\rho\delta(x,y,z) - g_{xx}^{EJ}(x,y,z)\right) * \left[i(x)\chi_{\text{dip}}(x) j_t(y,z)\right] \quad (4.31)$$

where δ is the Dirac delta. By projecting (4.31) on $\tilde{j}_t(y,z)$ defined in (4.20) over the cross-section A by using the inner product in (4.14), the right-hand side of can be written as

$$\iint_A \left[\int_{-\infty}^{+\infty} \iint_A \left(\rho\delta(x-x',y-y',z-z') - g_{xx}^{EJ}(x-x',y-y',z-z')\right) \times i(x')\chi_{dip}(x') j_t(x',y') dx'dy'dz'\right] \tilde{j}_t^*(y,z) dydz. \quad (4.32)$$

By switching the integration order, and by closing the integrals in the cross section, one can define the transverse Green's function as follows

$$\int_{-\infty}^{+\infty} d(x-x')\, i(x')\chi_{\text{dip}}(x')dx' = \int_{-\infty}^{+\infty} \left\{\rho\delta(x-x')\langle j_t, \tilde{j}_t\rangle_A - \iint_A \iint_A g_{xx}^{EJ}(x-x',y-y',z-z') j_t(x',y') \times dy'dz'\, \tilde{j}_t^*(y,z) dydz\right\} i(x')\chi_{\text{dip}}(x')dx'. \quad (4.33)$$

By equating (4.33) to the projected left-hand side of (4.31), one can write as follows

$$V_0 f^{\Delta}(x)\langle e_t, \tilde{j}_t^*\rangle_A - V_{\text{end}} f^{\text{end}}(x)\langle e_t, \tilde{j}_t^*\rangle_A = \int_{-\infty}^{+\infty} d(x-x')\left[i(x')\chi_{\text{dip}}(x')\right]dx'. \quad (4.34)$$

By performing the Fourier transform of (4.34) with respect to x, one can write the following expression

$$V_0 F^{\Delta}(k_x)\langle e_t, \tilde{j}_t^*\rangle_A - V_{\text{gap}} F^{\text{end}}(k_x)\langle e_t, \tilde{j}_t^*\rangle_A = D(k_x)\left[X_{\text{dip}}(k_x) * I(k_x)\right] \quad (4.35)$$

where F^{Δ}, I, X_{dip}, F^{end}, and D are the Fourier transforms of f^{Δ}, i, χ_{dip}, f^{end}, and d, respectively. By assuming that e_t has a unitary integral on the cross-section, the spectrum of the current can be finally written as follows

$$X_{\text{dip}}(k_x) * I(k_x) = \frac{V_0 F^{\Delta}(k_x) - V_{\text{end}} F^{\text{end}}(k_x)}{D(k_x)}. \quad (4.36)$$

4.2.2 Field Representation

The modelling of the incident field and of the transverse current distribution are congruent with those of [6], allowing to calculate the transverse Green's function with the procedures of [6]. These use the spectral domain Green's function, which allows the efficient handling of dipoles in layered media.

Fig. 4.4, show that the x-component of electric field decays along x for $|x| > \ell/2$. Accordingly the two-sided longitudinal field distribution are assumed, for the sake of simplicity, to have the following exponential behaviour

$$f^{\text{end}}(x) = \frac{1}{2c}\left(e^{-\frac{x-\ell/2}{c}}u(x-\ell/2) + e^{\frac{x+\ell/2}{c}}u(-x-\ell/2)\right) \tag{4.37}$$

with u being the unitary step function and c the decay rate, whose value has been determined empirically from CST simulations. For dipoles in free space or located between free space and a dielectric, $c = \lambda_0/40$ (where λ_0 is the free-space wavelength at each operating frequency) provides accurate results regardless of the specific the geometry. By calculating the Fourier transform of (4.37), one obtains the following spectrum

$$F^{\text{end}}(k_x) = \frac{1}{2}\left(\frac{e^{jk_x\ell/2}}{1-jk_xc} + \frac{e^{-jk_x\ell/2}}{1+jk_x}\right) \tag{4.38}$$

which is used to calculate the current spectrum with (4.36).

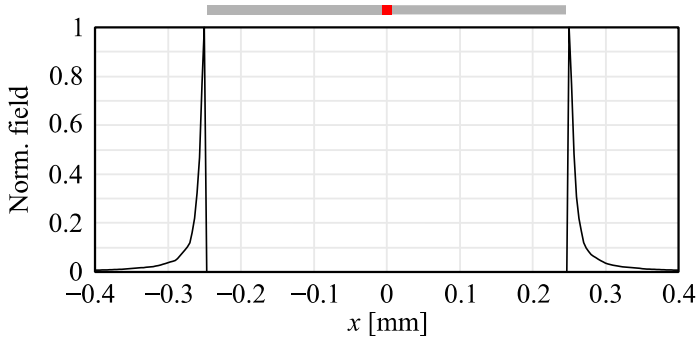

Fig. 4.4. Normalized x-component of the electric filed after the endpoints of the dipole obtained with a CST simulation.

4.2.3 Method of Moments Solution

The spectrum (4.36) has only been formally defined as the weight V_{end}, given the excitation V_0, has still to be determined to calculate the current spectrum of each specific problem. The current distribution $i(x)$ can be obtained from (4.36). with the following inverse Fourier transform

$$\frac{1}{2\pi}\int_{-\infty}^{+\infty}\left[X_{\text{dip}}(k_x) * I(k_x)\right]e^{-jk_xx}dk_x = \frac{1}{2\pi}\int_{-\infty}^{+\infty}\frac{V_0F^{\Delta}(k_x) - V_{\text{end}}F^{\text{end}}(k_x)}{D(k_x)}e^{-jk_xx}dk_x. \tag{4.39}$$

The left- and right-hand side of (4.39) can be projected on $t(x)$ as follows

$$\int_{-\infty}^{+\infty}\left\{\frac{1}{2\pi}\int_{-\infty}^{+\infty}\left[X_{\mathrm{dip}}(k_x)*I(k_x)\right]e^{-jk_xx}dk_x\right\}t^*(x)dx$$
$$=\int_{-\infty}^{+\infty}\left\{\frac{1}{2\pi}\int_{-\infty}^{+\infty}\frac{V_0F^{\Delta}(k_x)-V_{\mathrm{end}}F^{\mathrm{end}}(k_x)}{D(k_x)}e^{-jk_xx}dk_x\right\}t^*(x)dx. \tag{4.40}$$

and by exchanging the integration order, (4.40) can be written as follows

$$\frac{1}{2\pi}\int_{-\infty}^{+\infty}\left(\int_{-\infty}^{+\infty}t^*(x)e^{-jk_xx}dx\right)\left[X_{\mathrm{dip}}(k_x)*I(k_x)\right]dk_x$$
$$=\frac{1}{2\pi}\int_{-\infty}^{+\infty}\left(\int_{-\infty}^{+\infty}t^*(x)e^{-jk_xx}dx\right)\frac{V_0F^{\Delta}(k_x)-V_{\mathrm{end}}F^{\mathrm{end}}(k_x)}{D(k_x)}dk_x \tag{4.41}$$

where the integrals in brackets can be recognized as the Fourier transforms of t^*, and yielding

$$\frac{1}{2\pi}\int_{-\infty}^{+\infty}\left[X_{\mathrm{dip}}(k_x)*I(k_x)\right]T(-k_x)dk_x$$
$$=V_0\left[\frac{1}{2\pi}\int_{-\infty}^{+\infty}T(-k_x)\frac{F^{\Delta}(k_x)}{D(k_x)}dk_x\right]$$
$$-V_{\mathrm{end}}\left[\frac{1}{2\pi}\int_{-\infty}^{+\infty}T(-k_x)\frac{F^{\mathrm{end}}(k_x)}{D(k_x)}dk_x\right] \tag{4.42}$$

where T is the Fourier transform of t. By considering t either f^{Δ} or f^{end}, the following two unknown linear system can be obtained

$$\begin{cases}V_0Y_{\Delta,\Delta}-V_{\mathrm{end}}Y_{\Delta,\mathrm{end}}=I_0\\V_0Y_{\Delta,\mathrm{end}}-V_{\mathrm{end}}Y_{\mathrm{end},\mathrm{end}}=I_{\mathrm{end}}\end{cases}. \tag{4.43}$$

where I_0 and I_{end} are the average currents on the gap and on the space after the dipole terminations. The admittances are defined as follows

$$Y_{m,n}=\frac{1}{2\pi}\int_{-\infty}^{+\infty}\frac{F^m(k_x)F^n(-k_x)}{D(k_x)}dk_x \tag{4.44}$$

with m and n being either "Δ" or "end". After having imposed an open-circuit condition outside the dipole, i.e., $I_{\mathrm{end}}=0$, I_0 and V_{end} can be analytically calculated as follows

$$V_{\mathrm{end}}=V_0\frac{Y_{\Delta,\mathrm{end}}}{Y_{\mathrm{end},\mathrm{end}}}$$
$$I_0=V_0\left(Y_{\Delta,\Delta}-\frac{Y_{\Delta,\mathrm{end}}^2}{Y_{\mathrm{end},\mathrm{end}}}\right). \tag{4.45}$$

The expression of V_{end} can be used to calculate the current spectrum in (4.36), and I_0 can be used to calculate the input impedance, starting from its definition and calculated as follows

$$Z_{\mathrm{in}} = \frac{V_0}{I_0} = \frac{Y_{\mathrm{end,end}}}{Y_{\Delta,\Delta} Y_{\mathrm{end,end}} - Y_{\Delta,\mathrm{end}}^2}. \tag{4.46}$$

4.3 Validation and Results

The spectral domain formulation allows the efficient analysis of dipoles having cross-sections that are small in terms of the dimensions of the surrounding dielectrics and also Δ-gaps, which are in the order of hundredths of wavelengths. Moreover, as the transverse Green's function $D(k_x)$ depends only on the transverse geometry, dipoles having different lengths ℓ and different gap sizes Δ can be studied from the same integrals over the cross-section. Within this work, we present the validation and the results, in terms of the input impedance and current distribution.

4.3.1 Input Impedance

The input impedance can be calculated using (4.46), and an example is shown in Fig. 4.5(a) and in Fig. 4.5(b), where a fair agreement with CST is obtained. However, when the capacitance of the gap becomes significant, i.e. the cross section is much wider than the feeding gap, the present method starts to become accurate at high frequencies. In these cases, the capacitance if the gap is underestimated in $Y_{\Delta,\Delta}$, because the transverse current distribution $j_t(y,z)$ is distributed only on the edges of the two faces of the feeding gap instead of being uniform. Therefore, an additional parallel capacitance is needed to compensate for this effect. This can be simply calculated as a parallel plate as $C = \varepsilon_0 \varepsilon_{\text{eff}} w_y w_z / \Delta$. This compensation is used in Fig. 4.5(c), improving the comparison with CST. It is worth mentioning that, as the added capacitance does not affect the interaction between the dipole and the lens, it is irrelevant for the synthesis of the auxiliary dipole in the auxiliary source method explained in Chapter 3.

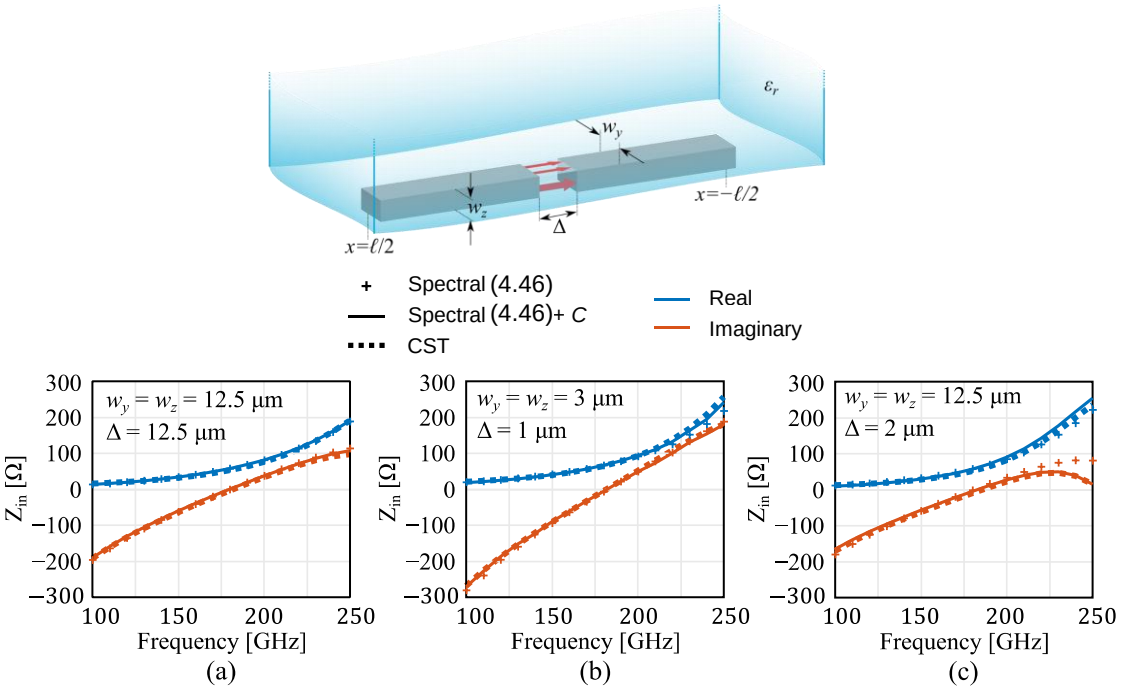

Fig. 4.5. Input impedance of a dipole having length $l = 500$ µm, printed between free space and a dielectric of permittivity $\varepsilon_r = 4$ and (a) width $w_y = 12.5$µm, thickness $w_z = 12.5$µm, fed by a gap long $\Delta = 12.5$µm, (b) width $w_y = 3$µm, thickness $w_z = 3$µm, fed by a gap long $\Delta = 1$µm, and (c) width $w_y = 12.5$µm, thickness $w_z = 12.5$µm, fed by a gap long $\Delta = 2$µm.

4.3.2 Current Distribution

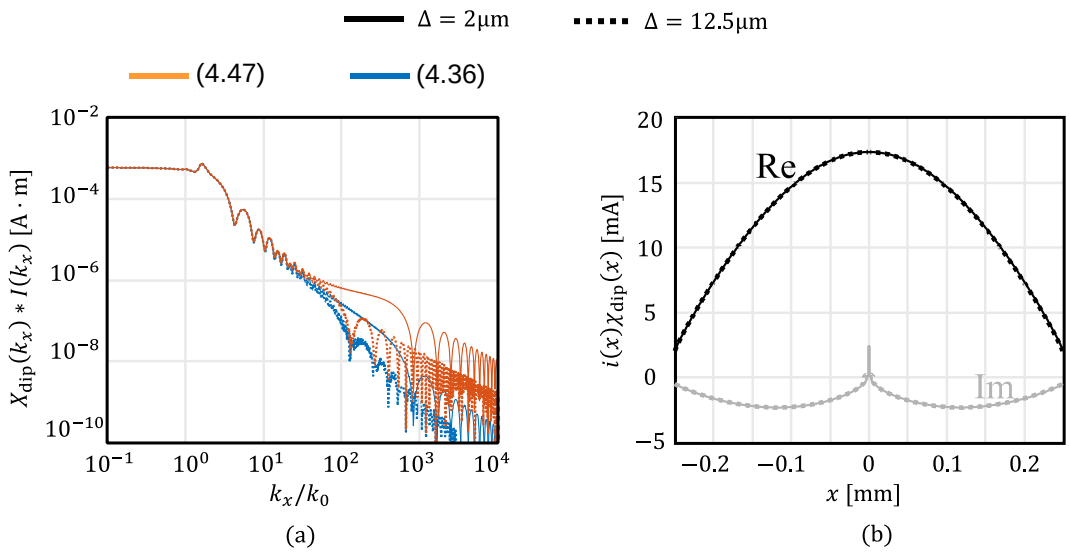

Fig. 4.6. (a) Spectrum of and (b) Spatial distribution of the current at 180 GHz of a dipole having length $l = 500\mu\mathrm{m}$, width and thickness $w_y = w_z = 12.5\mu\mathrm{m}$, printed between free-space and a semi-infinite dielectric with relative permittivity $\varepsilon_r = 4$, and excited with $V_0 = 1\mathrm{V}$ by a Δ-gap generator

As the capacitor has an impact on the current distribution and its spectrum, (4.36) has to be corrected with an additional term as follows

$$X_{\mathrm{dip}}(k_x) * I(k_x) = \frac{V_0 F^{\Delta}(k_x) - V_{\mathrm{end}} F^{\mathrm{end}}(k_x)}{D(k_x)} + \frac{j\omega C V_0 F^{\Delta}(k_x)}{\Delta} \tag{4.47}$$

Where $j\omega C V_0$ models the current flowing on the capacitor given the excitation V_0. The function F^{Δ} models the confinement of the displacement currents within the source region, assuming them to be uniformly distributed. An example of the spectrum is given in Fig. 4.6(a), where the spectra (4.36) and (4.47) are compared at 180GHz for dipoles $l = 500\mu\mathrm{m}$, having a cross-section $w_y = w_z = 12.5\mu\mathrm{m}$, printed between free-space and a semi-infinite media of relative permittivity $\varepsilon_r = 4$ and excited with $V_0 = 1\mathrm{V}$. The effect of the capacitance C in (4.47) is to place an high frequency component, depending on Δ, while leaving untouched the spectrum around k_0. The current distribution in the spatial domain is calculated by performing the inverse Fourier transform of (4.47), and an example related with the previous study case is shown in Fig. 4.6(b). One notices that the real part results unaffected by the different size of the feeding gap, the imaginary part peaks in correspondence of the source region when reducing Δ.
The farfield patterns on the upper hemisphere at 180 GHz for the case Fig. 4.5(a) are shown in Fig. 4.7. These are calculated with the following far-field asymptotic evaluation

$$\vec{E}(r_{\mathrm{obs}}, \theta_{\mathrm{obs}}, \phi_{\mathrm{obs}}) \approx j k_{zd,\mathrm{obs}} \hat{I}(k_{xd,\mathrm{obs}}) J_{ty}(k_{yd,\mathrm{obs}}) \frac{e^{-jkr}}{2\pi r} \times \int_0^{w_z} j_{tz}(z')\, \bar{\bar{G}}^{EJ}(k_{xd,\mathrm{obs}}, k_{yd,\mathrm{obs}}, z, z') \cdot \hat{x}\, dz' \tag{4.48}$$

Differently form the standard case, the metal thickness is included considering the superposition of current layers at different heights, having an amplitude profile given by $j_{t,z}(z')$. The spectrum $\hat{I}$ in k_x has been windowed starting from (4.47) as in [20].

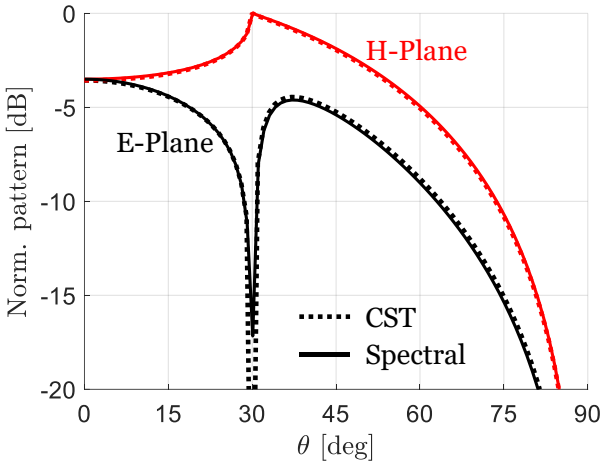

Fig. 4.7. Farfield patterns at 180 GHz of a dipole having length $l = 500\ \mu\text{m}$, printed between free space and a dielectric of permittivity $\varepsilon_r = 4$ and (a) width $w_y = 12.5\mu\text{m}$, thickness $w_z = 12.5\mu\text{m}$, fed by a gap long $\Delta = 12.5\mu\text{m}$.

5 Conclusions

5.1 Summary

The core of the thesis is Chapter 3, where a novel method to study integrated lens antenna is proposed. As the feed of the antenna is characterized by fine details, much smaller than its surroundings, the use of a full-wave solver makes the analysis excessively long. Moreover, if the solver is based on a structured mesh, the simulation becomes prohibitive due to excessive unknowns. The main idea behind the method proposed in this thesis is to decouple the analysis of the feed from the interaction between the feed and the lens. For this purpose, the reflection from the lens can be extracted by using an auxiliary feed, which has the same radiating currents as the original feed but has a coarser representation. Once the reflections from the lens have been extracted and the input impedance of the original feed in the absence of the reflections is known, the total input impedance of the original feed illuminating the lens can be reconstructed. The synthesis of the auxiliary feed and the extraction of the reflection is carried out with the Volumetric Method of Moments (V-MoM), while the analysis of the original feed in the absence of the reflections can be conducted with different techniques, such as CST or, in the case of a dipole, in the spectral domain.
As one of the main tools used in this thesis is the V-MoM developed in the THz sensing group, an overview of this full-wave solver is given in Chapter 2. The V-MoM solves the Electric Filed Integral Equation (EFIE), obtained with the volume equivalence theorem, by decomposing the incident and scattered field with piece-wise constant basis functions organized in a structured grid. The EFIE is then converted into a linear system, whose solution is found with the conjugate gradient (CG) iterative method. Thanks to the structured grid, the matrix of the linear system assumes a Toeplitz form, which allows us to calculate the matrix product with the FFT by reducing the computational time and the number of stored elements.
In the case of a dipole-fed lens, the feed embedded in a stratified media can be analyzed in the spectral domain. For this purpose, an analytical method to calculate the input impedance and the current distribution of a finite dipole is proposed in Chapter 4. This method is based on the Green's function of an infinite dipole where, differently from previous analysis, the dipole is not assumed to be infinitesimally thick, and the actual geometry of the conductor is considered. The finiteness of the dipole is taken into account with an additional incident field at the terminations of the dipole, and an extra term is added to the input impedance to represent the capacitance of the feeding gap. The advantages of this method are multiple: not only it gives a solution much faster than the common full-wave solvers such as CST, but it also provides insight into the different spectral components of the currents flowing on the dipole.

5.2 Future Work

5.2.1 Improvement of the V-MoM

The theoretical background of the extraction of the reflections with the auxiliary source method has been proposed, but it has been applied to a simplified stratification consisting of a feed radiating at the interface between free-space and a homogeneous media.

However, integrated lens antennas are based on more complicated stratifications, which also include a ground plane. This means that the synthesis of the auxiliary feed, which is carried out with the V-MoM, should be extended to more complex stratification.
Moreover, the computation time increases with the permittivity and the size of the dielectric (see Table 3). To address this issue, the number of iterations required by the iterative solvers can be reduced by applying a preconditioner to the linear system.

5.2.2 Improvement of the Spectral Dipole

In Chapter 4, it is shown that the transverse current distribution chosen to build the dipole Green's function fails to represent the capacitive feeding gap, underestimating its value. To compensate for this deficiency, a parallel plate capacitor with the same dimension as the feeding gap has been added to the input impedance. A deeper analysis of the behaviour of the current near the feeding gap should be conducted by, for example, including a different transverse distributions on the feeding gap.
On top of that, the spectral analysis of a dipole should be extended to an array of dipoles, as they are commonly used to illuminate the lens.

6 Bibliography

[1] CST Studio Suite, Dassault Systèmes, Vélizy-Villacoublay, France,2023.

[2] R. Ozzola, J. Geng, N. Llombart, A. Freni, D. Cavallo, and A. Neto, “A volumetric method of moments for integrated lens antennas,” in 2022 47th International Conference on Infrared, Millimeter and Terahertz Waves (IRMMW-THz), IEEE, 2022, pp. 1–2.

[3] J. Volakis and K. Sertel, Integral Equation Methods for Electromagnetics, ser. Electromagnetic Waves. Institution of Engineering and Technology, 2012.

[4] R. F. Harrington and J. L. Harrington, Field computation by moment methods. Oxford University Press, Inc., 1996.

[5] M. Hestenes and E. Stiefel, "Methods of Conjugate Gradients for Solving Linear Systems," Journal of Research of the National Bureau of Standards, vol. 49, no. 6, pp. 409-436, Dec 1952

[6] E. Speksnijder, R. Ozzola, A. Neto, “Spectral Domain Green’s Function of an infinite dipole with non-zero metal thickness and rectangular cross-section,” *IEEE Trans. Microw. Theory Tech.*, to be published. doi:10.1109/TMTT.2024.3361532.

[7] E. Speksnijder, “Development of spectral domain techniques for the analysis of printed transmission lines with nonzero conductor thickness,” M.S. thesis, ME, TU Delft, Delft, Netherlands, 2023. [Online]. Available: https://repository.tudelft.nl/islandora/object/uuid:f5c2accc-7c31-4f89-84c0-03735fc7de31/datastream/OBJ/download

[8] L. Sun and W. C. Chew, “A novel formulation of the volume integral equation for electromagnetic scattering,” Waves in Random and Complex Media, vol. 19, no. 1, pp. 162–180, 2009.

[9] A. G. Polimeridis, F. Vipiana, J. R. Mosig, and D. R. Wilton, “DIRECTFN: Fully numerical algorithms for high precision computation of singular integrals in galerkin SIE methods,” *IEEE Trans. Antennas and Propag.*, vol. 61, no. 6, pp. 3112–3122, Jun. 2013.

[10] A. A. Tambova, M.S. Litsarev, G. Guryev, and A. G. Polimeridis, “On the generalization of DIRECTFN for singular integrals over quadrilateral patches,” IEEE Trans. Antennas Propag., vol. 66, no. 1, pp. 304-314, Jan. 2018.

[11] J. Schäfer. (2016) Matscat. [Online]. Available: https://nl.mathworks.com/matlabcentral/fileexchange/36831-matscat?tab=reviews%2F2100233

[12] H. Zhang, S. Bosma, A. Neto, and N. Llombart, “A dual-polarized 27 dBi scanning lens phased array antenna for 5G point-to-point communications,” *IEEE Trans. Antennas and Propag.*, vol. 69, no. 9, pp. 5640–5652, Sept. 2021.

[13] N. van Rooijen, M. Alonso-delPino, M. Spirito, and N. Llombart, “Core-shell leaky-wave lens antenna for 150GHz fly’s eye communication systems,” presented at the 16th European Conference on Antennas and Propagation (EuCAP), Madrid, Spain, Mar. 27-Apr. 1, 2022.

[14] J. Geng, “Volumetric method of moments: a numerical tool for high frequency problems analysis,” M.S. thesis, ME Dept. Delft University of Technology, Delft, The Netherlands, 2022.

[15] H. Zhang, S. O. Dabironezare, G. Carluccio, A. Neto, and N. Llombart, “A Fourier optics tool to derive the plane wave spectrum of quasi-optical systems [EM

programmer's notebook]," *IEEE Antennas Propag. Mag.*, vol. 63, no. 1, pp. 103-116, Feb. 2021.

[16] D. Cavallo, W. H. Syed, and A. Neto, "Equivalent transmission line models for the analysis of edge effects in finite connected and tightly coupled arrays," *IEEE Trans. Antennas and Propag.*, vol. 65, no. 4, pp. 1788–1796, 2017.

[17] R. M. van Schelven, D. Cavallo and A. Neto, "Equivalent Circuit Models of Finite Slot Antennas," *IEEE Trans. Antennas and Propag.*, vol. 67, no. 7, pp. 4367-4376, July 2019.

[18] A. Neto and S. Maci, "Green's function for an infinite slot printed between two homogeneous dielectrics. I. Magnetic currents," *IEEE Trans. Antennas and Propag.*, vol. 51, no. 7, pp. 1572-1581, Jul. 2003.

[19] A. Neto and S. Maci, "Input impedance of slots printed between two dielectric media and fed by a small Δ-gap," *IEEE Antennas Wirel. Propag. Lett.*, vol. 3, pp. 113-116, 2004.

[20] A. J. van Katwijk, A. Neto, G. Toso, and D. Cavallo, "Efficient semi-analytical method for the analysis of large finite connected slot arrays," *IEEE Trans. Antennas and Propag.*, vol. 71, no. 1, pp. 402-410, Jan. 2023.